Upscaling of Reactive Mass Transport through Porous Electrodes in Aqueous Flow Batteries

Jakub K. Wlodarczyk,[1,z] Roman P. Schärer,[1] K. Andreas Friedrich,[2,3] and Jürgen O. Schumacher[1]

[1]*Institute of Computational Physics, Zurich University of Applied Sciences, 8400 Winterthur, Switzerland*
[2]*German Aerospace Center (DLR), Institute of Engineering Thermodynamics, Electrochemical Energy Technology, 70569 Stuttgart, Germany*
[3]*Institute of Building Energetics, Thermal Engineering and Energy Storage (IGTE), University of Stuttgart, 70569 Stuttgart, Germany*

Porous electrodes (PEs) are an important component of modern energy storage devices, such as lithium-ion batteries, flow batteries or fuel cells. Their complicated multiphase structure presents a considerable challenge to modeling and simulation. In this paper, we apply the volume-averaging method (VAM) as an efficient approach for the evaluation of effective macroscopic transport parameters in PEs. We consider the transport of electro-active species coupled to heterogeneous Butler-Volmer type reactions at the electrode surface. We identify the characteristic scales and dimensionless groups for the application to aqueous flow batteries. We validate the VAM-based model with direct numerical simulation results and literature data showing excellent agreement. Subsequently, we characterize several simplified periodic PE structures in 2D and 3D in terms of hydraulic permeability, effective dispersion and the effective kinetic number. We apply the up-scaled transport parameters to a simple macroscopic porous electrode to compare the overall efficiency of different pore-scale structures and material porosity values over a wide range of energy dissipation values. This study also reveals that the Bruggeman correction, commonly used in macroscopic porous electrode models, becomes inaccurate for realistic kinetic numbers in flow battery applications and should be used with care.

Symbols and Acronyms

Acronym	Explanation
1D, 2D, 3D	1,2,3-dimensional
BC	Boundary condition
BCC	Body-centered cubic
BV	Butler-Volmer
DNS	Direct numerical simulation
FB	Flow battery
FCC	Face-centered cubic
H	Hexagonal
LBM	Lattice Bolzmann method
LCOS	Levelized cost of storage
PDE	Partial differential equation
PE	Porous electrode
PEMFC	Proton-exchange membrane fuel cell
PNM	Pore-network model
REV	Representative elementary volume
SC	Simple cubic
VAM	Volume-averaging method
VFB	Vanadium flow battery
XCT	X-ray computed tomography

Latin Symbols

Symbol	Explanation
$A_{\beta\sigma}$	Interfacial surface between phases β and σ
$\mathcal{A}_{\beta\sigma}$	Interfacial surface area between phases β and σ
a_a, a_c	Anodic and cathodic terms of the BV equation
a_v	Electrode specific surface area
c	Molar concentration
D	Diffusion coefficient
d	Fiber diameter
$\mathbf{D}^{\text{eff}}$	Effective diffusion tensor
$\mathbf{D}^*$	Total dispersion tensor
E	Electrode polarization
E_{eq}	Equilibrium potential
$\mathbf{e}^{(i)}$	ith unit basis vector
F	Faraday constant (96485 C mol^{-1})
$f = F/RT$	Inverse thermal voltage
f	Field variable
$\mathbf{f}, g$	Closure variables
j	Current density
j_0	Reference exchange current density
k	Heterogeneous reaction rate
$\mathbf{K}$	Permeability tensor
k_0', k_1'	Kinetic constants (variable transformation)
Ki	Kinetic number
n	Number of electrons transferred
$\mathbf{n}$	Unit vector
p	Pressure
Pe	Péclet number
R	Universal gas constant (8.3145 J mol^{-1} K^{-1})
$\mathbf{r}$	Position vector
r_i	Production term
Re	Reynolds number
s	Reaction rate
Sc	Schmidt number
T	Temperature
$\mathbf{v}$	Velocity
V	Unit-cell domain
$\mathcal{V}$	Total volume

Greek Symbols

Symbol	Explanation
α	Transfer coefficient
ε	Porosity
η_{ref}	overpotential with respect to a reference state
η^{diss}	Specific dissipation energy
η_S	Local surface overpotential
μ	Dynamic viscosity of the electrolyte
ν	Kinematic viscosity of the electrolyte
τ	Tortuosity

Subscripts

Symbol	Explanation
β	Liquid phase

[z]E-mail: j.wlod@protonmail.com

σ	Solid phase
red	Reduced species
ox	Oxidized species
ref	Reference
eq	Equilibrium
l	Nondimensionalization based on unit cell size
d	Nondimensionalization based on fiber diameter
M	Nondimensionalization based on macroscale parameters
T	Total
p	Particle

Superscripts

Symbol	Explanation
0	Characteristic quantity
$'$	Transformed variable
β	Refers to the liquid electrolyte phase
σ	Refers to the solid electrode phase
$\star$	Alternative formulation
i	Species i
a, c	Anodic, cathodic
BV	Refers to BV-type reaction
eff	Effective

Porous electrodes (PE) are ubiquitous in industrial electrochemistry, as they allow for the application of high currents, while maintaining a relatively compact size of the electrochemical reactor. Moreover, for certain energy storage devices in which the active material is incorporated into the electrode itself, utilising porous materials aids to increase not only their power density, but also energy density, like in the case of Li-ion batteries.

In recent years, one particularly interesting application of PE gained popularity in novel devices for large-scale energy storage, referred to as (redox) flow batteries (FB). Such industrial-scale systems, although being still an emerging technology, constitute one of the most promising solutions to the problem of electric grid instability, caused by a rapidly expanding share of intermittent renewable energy sources.[1,2] Flow battery technology is one of the main candidates for storing large amounts of electric energy on sites, where the construction of established grid imbalance-equalising solutions, such as pumped-hydro storage, is not feasible.

In contrast to Li-ion technologies, FBs promise long-duration storage capabilities (over 20 years) without considerable capacity loss.[1] This is due to the fact that the electro-active material in flow batteries is stored in tanks outside the battery stack. The electrolyte is brought in contact with non-reactive electrodes only for a short time by circulating it through an engineered, highly-porous and electrically conductive material (usually carbon-based) by means of forced convection (pumping).

The flow distribution inside such porous structures plays an important role in the overall performance of FB systems. This is less of an issue in Li-ion batteries, in which the electrolyte is quiescent and the main transport mechanism of lithium is diffusion and migration. In FBs, electrochemical reactions occur at the surface of a porous medium. Electro-active species dissolved in the electrolyte are transported in the liquid bulk and to/from the electrode surface by convection, diffusion and migration. In general, all of these phenomena are strongly coupled and highly non-linear, which largely complicates the theoretical description of FB operation.[3]

Modeling and simulation of electrochemical devices has become important not only for scientific investigations, but also for industrial product development and prototyping. In FBs, physical and chemical phenomena occur on a disparity of scales, ranging from electric double layer effects (nanometres), through stagnant diffusion layers (tenths of micrometres), up to cells, stacks and full systems (centimetres to metres).

To accurately simulate a FB cell (or, in principle any electrochemical flow cell, such as electrolyzers or electrochemical synthesis reactors), the impact of the PE microstructure needs to be carefully conveyed to larger-scale models in the process of increasing the model abstraction.[3] In the upscaling process, however, not all information from the pore-scale is retained in the macroscopic formulation (e.g. volume-averaging filters only the relevant information). Simulating an entire macroscopic cell using the full microscale pore resolution would require prohibitively large computational resources, even for modern computer clusters. Instead, various upscaling techniques can be employed to incorporate essential pore-scale related properties into macroscopic cell models.

In this paper we investigate the application of the volume-averaging method to the simulation of PEs with convective and diffusive mass transport coupled to a Butler-Volmer (BV) type heterogeneous reaction at the electrode surface. Here we consider simplified, periodic PE geometries at the pore-scale with a focus on studying the effect of the pore-scale geometry on macroscopic transport properties. After presenting the dimensional analysis and upscaling methodology we show verification results of the effective transport parameters against published results. We then discuss the effective transport properties, such as the dispersion and effective reaction rate of several simplified pore-scale geometries. We highlight modeling errors that result from often-used oversimplified analytical solutions in cell-scale FB models. Finally, we present the application of the effective material properties to the mass transport of electro-active species through a macroscopic electrode, where the pore-scale geometries are compared in terms of the resulting energy dissipation and overall reaction rate allowing for an assessment of the overall efficiency of the porous materials.

State of The Art

***Porous electrodes applied to flow batteries.—** The big picture.—* In a FB, energy is stored in fluids (electroactive solutions, suspensions, gases) that are kept in external reservoirs. The fluids are forced through a battery stack, in which PEs are enclosed and sealed. The electrolyte comes into contact with the surface of the PE at the micro-scale, where reversible charge transfer occurs, allowing for discharging and charging of the FB. PEs directly determine the battery performance: not only do they provide active sites for electrochemical reaction, but also paths for electrolyte mass transport and electronic conduction (current collection).[4] PEs also play a crucial role in determining the mechanical properties of a stack. When subjected to mechanical compression, PEs deform, influencing the transport properties such as the contact resistance between the bipolar plates and the PEs.

Currently, high cost of storage is one of the main factors prohibiting the ubiquitous spread of FB technology on the market. Thus, to lower the levelized cost of storage (LCOS), it is highly desired to design more robust FB systems with superior characteristics: higher power density, reduced system size, and competitive round-trip efficiency.[1]

In fact, re-designing, engineering and optimisation of FB electrodes is one of the core ideas toward improving the battery performance. Focusing on PE only, two main performance enhancement methods can be distinguished.[5] On the one hand, the fibers' surface may be functionalized with deposited nanomaterials (e.g. carbon nanorods) or thermal pre-treatment. The fiber precursor itself may also be changed (polyacrylonitrile, rayon, biomass), producing fiber characteristics dissimilar to that in commercial materials. Such methods can enhance their electrochemical performance, increase stability and surface area, and tailor specific properties, leading to improved efficiency in energy storage or conversion processes.[5] On the other hand, the morphology of the PE can be varied, such that desired structural features appear in a cascade of length scales. In this paper, we turn our attention to computationally analyze the latter idea.

Engineered pore structures can help to approach the ideal electrolyte transport process: convection to meso-scale pores through micro-scale pores, then diffusion into nanoscale pores and heterogeneous reaction.[4,6] Such gradient-pore oriented graphite felt, manufactured with pore sizes spanning from nano- to micro-scales, has demonstrated improved energy efficiency of a vanadium flow battery (VFB) by nearly 20%, compared to pristine graphite felt electrodes.[4] Novel materials with gradients of porosity within their volumes were found to be capable of delivering 69% higher discharge capacity than conventional VFB electrode design.[7]

Key metrics of porous electrodes.—Porous materials, whether natural or synthesized, are characterized by a complicated morphology of the solid material and the complementary void volume through which the electrolyte flows. The geometry, connectivity and orientation (topology) of these domains are typically disordered. Thus, these porous domains can be analyzed in terms of statistical descriptions.

The most fundamental geometric property of a porous electrode is porosity $\varepsilon \in (0, 1)$, which is the ratio of void volume to the total volume of the porous material. The total geometric surface area of the void-matrix interface divided by the total volume which encloses this surface is referred to as specific surface area, a_v (m^2 m^{-3}). The surface area available for redox reactions may in principle be different from the geometric one due to e.g. steric effects of the molecules.[8] Tortuosity, τ, is another often-used parameter, which describes the length of the effective path of transport (of mass, charge, heat, etc.) across the PE divided by the geometric distance.

Porosity, tortuosity and specific surface are, as expected, correlated.[9] In macroscopic electrode models, the tortuosity factor is often defined as[8]

$$D^{\text{eff}} = D\frac{\varepsilon}{\tau}, \qquad [1]$$

where D denotes the molecular diffusivity and D^{eff} is the effective diffusivity at the macroscale, which depends on the pore-scale morphology and transport processes. The well-known Bruggeman relation for random porous media used for more than 50 years is given by

$$\tau = \varepsilon^{-1/n}, \qquad [2]$$

where $n = 1$ for materials composed of randomly distributed cylinders and $n = 2$ for spheres.[8] Thanks to its simplicity, the Bruggeman relation has been used extensively in FB modeling literature (cf. e.g.[10–12]). We note that there exists an abundance of other correlations, see e.g.[13]

Despite the popularity of the Bruggeman approach in the porous electrode theory literature, experimental studies on Li-ion batteries indicate great deviations of tortuosity values predicted by Eq. 2 from measured data due to the complexity of the porous structures.[9] There are numerous reasons for this discrepancy. First, real PEs are characterized by a range of tortuosities, rather than a single, average value. Moreover, microstructural variations can locally increase the tortuosity by a factor of three.[14] Other explanations are sought in randomness in particle (solid matrix) packing and local non-homogenities. The Bruggeman relation was originally derived assuming spherical obstruction to transport,[8] whereas porous electrodes in FB consist of oblong fibers, which casts further doubts on the applicability of this relation to FB modeling. To date, no good correlation between microstructure and macroscopic tortuosity has been found.[9]

Incorporating meso- and micro-scale effects into component, stack and cell-types of models is vital not only for increasing model predictability, but also for improving the understanding of processes occurring within PEs.[15] Current techniques allow for manufacturing PEs with well-controlled micro- and nanostructure features. The remaining question persists: what is the optimal pore architecture to maximize power efficiency?[15]

Established methods for simulating porous electrodes.—*Continuum models with simplified closure relations.*—In the most typical FB modeling approach, the momentum, mass, heat and charge conservation equations are resolved in one to three spatial dimensions to virtually represent different parts of the flow cell or stack (e.g. flow fields, through-plane transport). The balanced quantities are treated as a macroscopic continuum (Newman-type[16] models), meaning that the governing equations are written for averaged (over the representative elementary volume, REV) dependent variables, rather than for their intrinsic (intra-pore) counterparts.[17,18] Transport properties (such as the diffusion coefficient or electrical conductivity) in the constitutive relations need to be corrected for the fact that the considered balanced quantities in liquid solution or gas phase (e.g. concentration) are in fact averaged over a domain consisting of both electrically conductive solid electrode phase (the so-called matrix) and void phase (taken by the liquid electrolyte or gas). However, such corrections are not particularly rigorous and only aim to better approximate the empirical data.

There are numerous examples of continuum modeling approaches using simplified relations for the transport parameters in the literature of FB modeling. For example Zhang et al.[2] simulated a VFB cell in 2D using the Brinkman equation for electrolyte flow with the Kozeny-Carman relation to estimate hydraulic permeability of the electrode, and the Bruggeman correction for diffusion coefficient and electric conductivity.

Albeit so common, such simple corrections of the intrinsic transport properties should be critically assessed, and the underlying assumptions verified for particular PE structures.[17,19] It is commonplace that microstructure parameters, such as porosity or specific surface area remain fitting parameters at the macroscopic level to better match model results with macroscopic observables (e.g. polarization curves).[20] Evidently, such an approach may jeopardize the predictive power of macroscopic continuum model simulations. To mitigate this problem, the evaluation of macroscopic transport properties via lower-scale electrode models is desired.

Pore-scale resolved models.—Pore-scale models of electrochemical energy devices have gained attention due to advancements in computational resources.[13,20] PEs have been studied using (1) direct numerical simulations (DNS) with common discretization methods, (2) lattice Boltzmann method (LBM), and (3) pore network models (PNM) for efficient meso-scale characterization.

In the first approach (1), X-ray computer tomography (XCT) is used to analyze a small part of a PE and a digital electrode geometry with solid and void voxels is reconstructed or a synthetic, computer-generated electrode morphology with structured or unstructured matrix fiber arrangement can be created.[21–23] The geometry is then discretized and a mesh is created to solve conservation law equations in both solid and void phases with numerical schemes (e.g. finite volume, element, or difference).[23–25]

In the LBM approach (2), fluid motion is modeled using a system of discrete mass distribution functions on a lattice. It has been applied in many fields including PEMFCs and FBs.[26–30] PNM models (3) simplify the complicated porous structure by approximating it with a network of voids connected by pores, preserving only the relevant mesostructure. This allows for rapid solutions of governing equations, even on single-core machines, at the cost of certain details being lost in the simplification process.[20,31,32]

Pore-scale models can estimate mass transport and effective transport properties, a valuable input for macrohomogeneous models, avoiding empirical correlations.[2] PE morphologies analyzed on sub-micrometre scale provide information on surface area, porosity, and tortuosity.[18,20] There is a trade-off between detail resolved by the DNS method and computational effort.

Up-scaling methods.—When dealing with the disparity of physical length scales in PEs, trade-offs must be sought to allow for obtaining accurate results at affordable computational costs. "Brute-force" modeling of the whole PE volumes (e.g. hundreds of cm^3) used in industrial FBs to resolve micrometre pores is impractical (or even impossible), due to prohibitively long computation times and memory usage. On the other hand, simulating FB electrodes using the computationally efficient macrohomogeneous approach requires additional subgrid-scale models to capture the electrode morphology effects on cell performance.

Mathematical upscaling methods can be used to rigorously determine the effective parameters in macroscopic transport equations, which reflect the effect of the pore-scale processes.[13,33] Various up-scaling methods exist and have been applied in numerous fields of science. All methods, however, share two common goals: (1) deriving macroscopic balance laws and (2) formulating closure problems for transport parameters to be used in the balance laws. In fact, many macroscopic models were first devised from empirical observations (e.g. Darcy's law, Brinkman equation) and only later derived using the formal mathematical upscaling.[34]

In this work, we develop a numerical tool to analyze porous electrode structures by means of VAM-based model, in which flow phenomena coupled to heterogeneous chemical or electrochemical reaction interface (of BV-type) occur. We focus particularly on the modeling of FBs, albeit the procedures discussed herein can be applied to other electrochemical flow cells, such as electrolyzers.

The VAM is used to derive spatially homogeneous representations of conservation laws in porous media. Processes in these media usually occur over various length scales, and the information from the smaller scale is systematically conveyed to the larger scale in the volume averaging process. This up-scaling procedure has been well documented in the literature[35–37] and applied in a variety of fields, for instance chemical engineering[38] or groundwater hydrology.[39]

Literature studies on the VAM most relevant for the application to FBs concern up-scaling of inertial and creeping flow in porous media,[40] dispersion of mass,[41] advection-diffusion-reaction equations (heterogeneous and homogeneous, zeroth and first order reactions),[37,42] and non-linear reactions: homogeneous[43] and heterogeneous.[44]

In the matter of electrochemistry, Le et al.[15] developed an up-scaled PE model of a chronoamperometric experiment, in which electron transfer was described using the BV equation and the mass transport at the pore-scale was assumed to be dominated by Fickian diffusion. Ultimately, however, the non-linear BV equation employed as the boundary condition in this study was simplified to a linear Tafel-like equation. For a given sufficiently high and constant overpotential, the surface reaction term was thus reduced to a first-order reaction. The authors used the VAM to derive effective parameters in representative, periodic PE consisting of spheres in simple cubic (SC), body-centered cubic (BCC) and face-centered cubic (FCC) geometric arrangements. The effective parameters resulting from the VAM were employed in a simplified 1D geometry to simulate the transient chronoamperometric response. The VAM results were then compared with a DNS of the same electrode structures and the agreement was excellent. Le et al. achieved roughly 3100 times speed-up of the 1D upscaled model compared to the DNS approach.

Model Outline

Transport phenomena within PEs are inherently of a multi-scale nature, as depicted in Fig. 1, where a hierarchy of scales is exhibited, starting from the macroscale in panel (A), over the mesostructure (B), the microstructure (C), to the surface phenomena (D).

We are interested in macroscopic transport models for PEs, which allow for the efficient simulation over large electrode domains with a characteristic length scale L. On the other hand, the pore-scale

structure has a characteristic length scale l, which is assumed to be much smaller compared to the macroscopic scale. By means of the VAM the effects of the pore-scale morphology and transport are incorporated into the macroscopic description.

In the VAM, the structure of micro-pores and the related phenomena (diffusion, migration in them) shown in panel (C) or surface phenomena schematized in panel (D) are commonly assumed[35] to be captured by a boundary condition (BC) at $A_{\beta\sigma}$, as designated in Fig. 2B.

Pore-scale transport modeling.—The electrode geometry is assumed to be rigid and spatially periodic, so that the electrode material is generated by translational copies of a periodic unit cell. In Fig. 2A we show an exemplary periodic porous electrode structure generated by a simple unit cell geometry displayed in Fig. 2B. The unit cell domain is partitioned into an electrode domain V_σ and electrolyte domain V_β, separated by an interface domain $A_{\beta\sigma}$.

At the pore-scale we assume the flow velocity to be small enough for inertial effects to be negligible. Furthermore, we assume dilute concentrations of the electro-active species. Assuming a Newtonian fluid, the convective flow can be described in terms of the Stokes equation

$$\nabla p - \nabla^2 \mathbf{v} = 0, \quad \nabla \cdot \mathbf{v} = 0, \quad \mathbf{r} \in V_\beta, \quad [3]$$

where p is pressure and $\mathbf{v}$ is the fluid velocity. We use no-slip boundary condition at the electrode surface.

To simplify the governing equations we assume the ohmic resistivity to be negligible both within the electrode material and the electrolyte phase. In practice, the latter condition can be realized experimentally by the usage of a supporting electrolyte. Additionally, the diffusion potential variation in the electrolyte bulk is assumed to be negligible. In this work we assume isothermal conditions and set the temperature to $T = 298.15$ K. Furthermore, we assume the average separation of the pore-scale electrode structures to be much larger compared to the Debye length, which allows to impose the electroneutrality condition within the electrolyte phase. These simplifications allow the mass transport of the electroactive species i to be described in terms of an advection-diffusion equation

$$\mathbf{v} \cdot \nabla c_i = D \nabla^2 c_i, \quad \mathbf{r} \in V_\beta, \quad [4]$$

where D denotes a diffusion coefficient, which is assumed to be constant and equal for all electro-active species. The coupling to the heterogeneous reactions at the electrode-electrolyte interface can be stated generally as

$$-D \nabla c_i \cdot \mathbf{n}_{\beta\sigma} = -r_i(c_1, \ldots, c_N), \quad \mathbf{r} \in A_{\beta\sigma}, \quad [5]$$

where $\mathbf{n}_{\beta\sigma}$ is the unit vector pointing from the electrolyte into the solid electrode phase (see Fig. 2B) and r_i denotes a general production term due to the electrochemical reaction.

Electrochemical reactions.—In the electrochemical context of this work, we consider the reversible one-electron transfer redox reaction

$$\text{Ox} + \text{e} \rightleftharpoons \text{Red}. \quad [6]$$

We model the kinetics of Reaction 6 using the "practical form"[45] of the Butler-Volmer equation

$$j = \frac{j_{0,\text{ref}}}{c_{\text{ref}}}(e^{(1-\alpha)f\eta_{\text{ref}}}c_{\text{red}} - e^{-\alpha f\eta_{\text{ref}}}c_{\text{ox}}), \quad [7]$$

where j is the current density at the electrode surface (A m^{-2}), c_{ref} denotes a fixed reference concentration (mol m^{-3}), α is the transfer coefficient, and
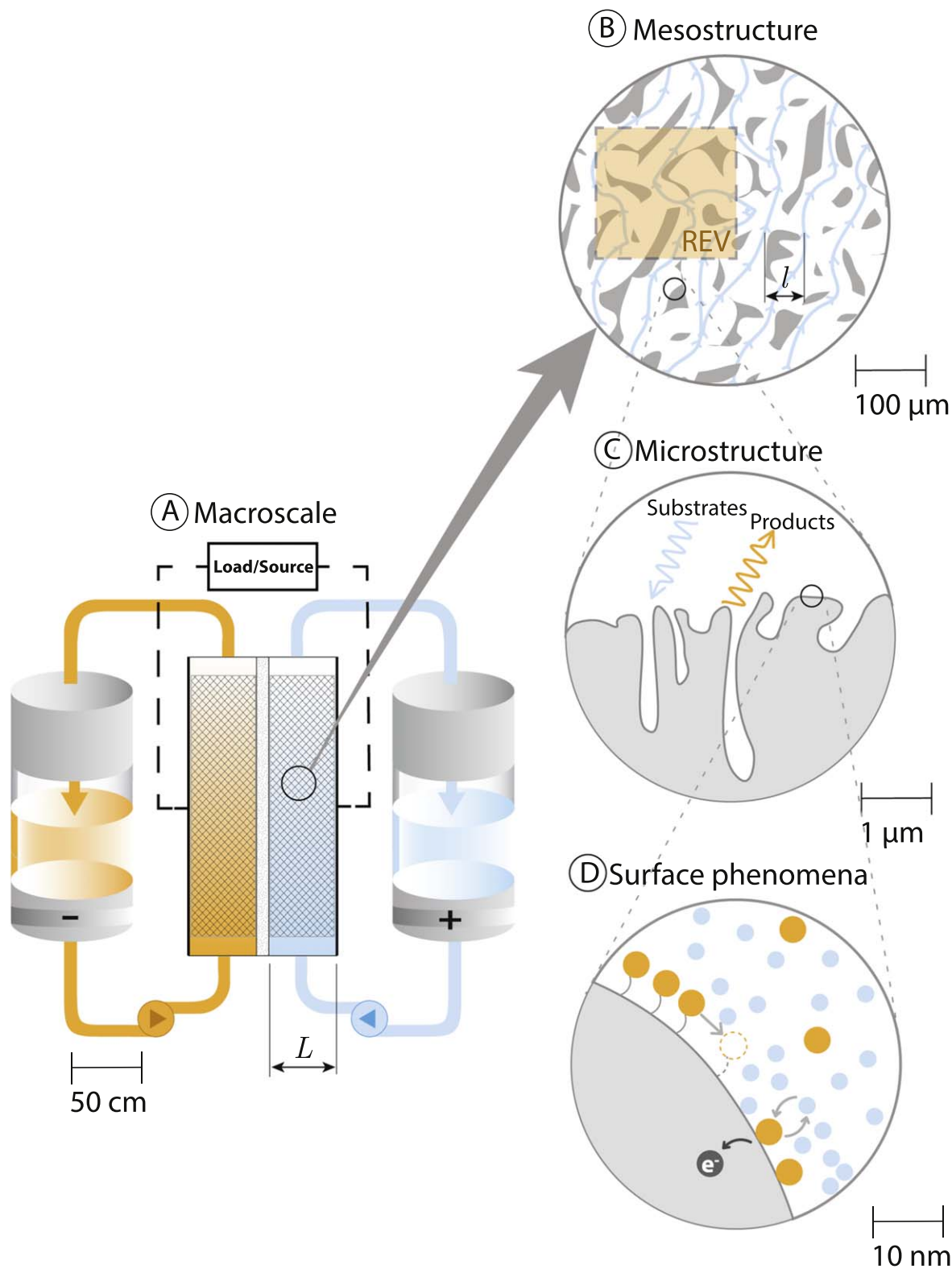
Figure 1. The cascade of length scales involved in FB models. A) Macro-scale featuring the characteristic macroscopic length scale L (practical modeling applications and system optimisation); B) Meso-scale structure featuring the characteristic pore-scale length l with the representative elementary volume (REV) of a simplified porous electrode with the characteristic length l at pore scale (e.g. fiber diameter); C) Micro-pore scale, where the dominant transport mode is molecular diffusion and migration in the electric field; D) Surface phenomena on the atomistic scale (e.g. adsorption, surface transport, EDL, catalyst degradation, electron exchange).
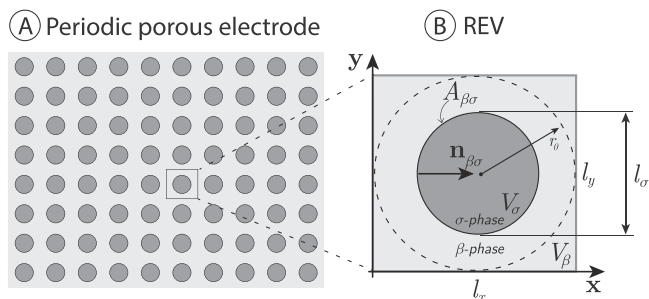
Figure 2. (A) Macroscopic representation of a simplified porous electrode—a periodic medium composed of conductive fibers, (B) the corresponding representative elementary volume.

$$j_{0,\text{ref}} = Fkc_{\text{ref}}, \quad \eta_{\text{ref}} = E - E_{\text{eq}}(c_{\text{ref}}), \quad f = \frac{F}{RT}, \qquad [8]$$

are the reference exchange current density, the overpotential with respect to a reference state, and the inverse thermal voltage (V^{-1}). In Eq. 8, k denotes the heterogeneous reaction rate constant (m s^{-1}), E is the electrode polarization (V), and E_{eq} is the equilibrium potential of the considered redox reaction.

Here we choose a reference state based on the reference inflow condition $c_{\text{ref}} = c_{\text{ox,ref}}^{\text{in}} = c_{\text{red,ref}}^{\text{in}}$ and assume for simplicity a symmetric reaction with $\alpha = 0.5$ in the rest of this work. In this work we adopt the convention that anodic currents and overpotentials have a positive sign.

Note that the local surface overpotential (measured just outside the double layer structure), $\eta_S = E - E_{\text{eq}}$, still depends in general on the local electrolyte composition, since E_{eq} is a function of the local species concentrations: Rewriting Eq. 7 in terms of the local surface overpotential yields

$$\eta_S = E - E_{\text{eq}} = E - E_{\text{eq,ref}} + \frac{1}{f}\ln\left(\frac{c_{\text{red}}}{c_{\text{ox}}}\right) \qquad [9]$$

with the current density

$$j = j_0(e^{(1-\alpha)f\eta_S} - e^{-\alpha f\eta_S}), \qquad [10]$$

where $j_0 = Fkc_{\text{red}}^{\alpha}c_{\text{ox}}^{(1-\alpha)} = j_{0,\text{ref}}(c_{\text{red}}/c_{\text{ref}})^{\alpha}(c_{\text{ox}}/c_{\text{ref}})^{(1-\alpha)}$ is the local exchange-current density.

Thanks to the assumption of negligible electrostatic potential gradients within the electrode and electrolyte bulk domains, the electrode polarization E is spatially constant along the electrode-electrolyte interface. Thus, according to Eq. 8 also the overpotential η_{ref} is constant. Therefore, for a given reference concentration, overpotential, and symmetry coefficient, the electric current density j is a linear function of the species concentrations. As we show in detail further below, this property allows to recast the BV equation to a linear reaction law

$$j = -Fkc_A \qquad [11]$$

corresponding to the reaction

$$A \rightarrow B. \qquad [12]$$

Characteristic scales and dimensionless groups.—In the following analysis it is convenient to cast all governing equations into their dimensionless equivalents. Such an approach has an advantage over dimensional formulation when working with a disparity of different scales as it reveals the dimensionless groups parametrising the physiochemical processes.

Let us introduce the nondimensional quantities

$$\bar{c} = \frac{c}{c^0}, \quad \bar{\mathbf{r}} = \frac{\mathbf{r}}{l^0}, \quad \bar{\mathbf{v}} = \frac{\mathbf{v}}{v^0}, \quad \bar{p} = \frac{p}{p^0},$$

$$\bar{j} = \frac{j}{j^0}, \quad \bar{\eta} = \frac{\eta}{V^0}, \quad \bar{E} = \frac{E}{V^0} \qquad [13]$$

defined with respect to the characteristic molar concentration c^0, length-scale l^0, velocity v^0, pressure p^0, current density j^0, and voltage V^0 given by

$$c^0 = c_{\text{ref}}, \quad l^0 = l_x, \quad v^0 = \frac{l^0 p^0}{\mu},$$

$$p^0 = l^0|\nabla\langle p\rangle^\beta|,$$

$$j^0 = \frac{DFc^0}{l^0}, \quad V^0 = \frac{RT}{F}, \qquad [14]$$

where $c_{\text{ref}} = 1$ mol L^{-1} is the characteristic species concentration, l_x denotes the size of a unit cell in the x-direction, $|\nabla\langle p\rangle^\beta|$ is the norm of the volume-averaged pressure gradient to be defined later, and V^0 is the thermal voltage.

One of the most important aspects of a dimensionless formulation is the identification of critical scaling parameters. Since for a given applied pressure difference the flow velocity is not known a priori, we define an alternative Reynolds number[40]

$$\text{Re}_l^\star = \frac{\rho(l^0)^3}{\mu^2}|\nabla\langle p\rangle^\beta| \qquad [15]$$

based on the applied pressure gradient, where ρ is the (constant) electrolyte density (kg m^{-3}) and μ denotes the (constant) dynamic viscosity (Pa s). Based on Re$_l^\star$, we define the Péclet number

$$\text{Pe}_l^\star = \frac{v^0 l^0}{D} = \text{Re}_l^\star\text{Sc}, \qquad [16]$$

where Sc $= \nu/D$ denotes the Schmidt number and $\nu = \mu/\rho$ is the kinematic viscosity of the electrolyte (m^2 s^{-1}). Since we consider here aqueous electrolytes, we set Sc $= 1000$ in the remainder of this work.

The transport of the electroactive species i in the β-phase is then described by the diffusion-advection equation given in nondimensional form as

$$\text{Pe}_l^\star\bar{\mathbf{v}}\cdot\bar{\nabla}\bar{c}_i = \bar{\nabla}^2\bar{c}_i, \quad \bar{\mathbf{r}} \in \bar{V}_\beta. \qquad [17]$$

The dimensionless scaling parameter controlling the importance of the electrochemical reaction with respect to diffusive transport is

$$\text{Ki}_l = \frac{kl^0}{D}. \qquad [18]$$

The nondimensional reactive boundary condition for the linear reaction law in Eq. 12 is then given by

$$-\bar{\nabla}\bar{c}_A\cdot\mathbf{n}_{\beta\sigma} = \text{Ki}_l\bar{c}_A, \quad \bar{\mathbf{r}} \in \bar{A}_{\beta\sigma}. \qquad [19]$$

Similarly, to cast the BV-type reaction given in Eq. 7 and the respective boundary condition into dimensionless form, we define the anodic and cathodic kinetic numbers as

$$\text{Ki}_l^a = \frac{kl^0}{D}a_a = \text{Ki}_l a_a, \quad \text{Ki}_l^c = \frac{kl^0}{D}a_c = \text{Ki}_l a_c \quad \text{with}$$

$$a_a = e^{(1-\alpha)f\eta_{\text{ref}}}, \quad a_c = e^{-\alpha f\eta_{\text{ref}}}, \qquad [20]$$

so that the dimensionless form of the BV equation reads

$$\bar{j} = \text{Ki}_l^a \bar{c}_{\text{red}} - \text{Ki}_l^c \bar{c}_{\text{ox}}, \quad \mathbf{r} \in A_{\beta\sigma} \qquad [21]$$

with the corresponding reactive boundary conditions

$$-\bar{\nabla}\bar{c}_{\text{red}} \cdot \mathbf{n}_{\beta\sigma} = \bar{j}, \quad -\bar{\nabla}\bar{c}_{\text{ox}} \cdot \mathbf{n}_{\beta\sigma} = -\bar{j}, \quad \mathbf{r} \in A_{\beta\sigma}. \qquad [22]$$

To simplify the notation we will drop the *overline* symbol in the following to denote nondimensional quantities.

Upscaling the transport equations.—In the VAM approach, the pore-scale transport equations are averaged over a REV (here corresponding to a unit cell) to derive the governing macroscopic transport equation and effective transport parameters.

We introduce the *intrinsic averaging operator* for any field variable f defined over the electrolyte domain V_β[35]

$$\langle f \rangle^\beta := \frac{1}{\mathcal{V}_\beta} \int_{V_\beta} f \, dV, \qquad [23]$$

where $\mathcal{V}_\beta = \int_{V_\beta} 1 \, dV$ is the volume of the liquid phase. The electrode porosity can be then expressed as $\varepsilon = \mathcal{V}_\beta / \mathcal{V}$, where $\mathcal{V}$ is the total unit-cell volume. Defining analogously the intrinsic averaging operator over the solid electrode domain V_σ allows to express the total volume as $\mathcal{V} = \mathcal{V}_\beta + \mathcal{V}_\sigma$.

In the process of VAM, f is decomposed into an intrinsic average, $\langle f \rangle^\beta$, and a spatial deviation, $\tilde{f}$, given by

$$f = \langle f \rangle^\beta + \tilde{f}, \qquad [24]$$

to which we shall return later.

Furthermore, we define the *superficial averaging operator* as:

$$\langle f \rangle := \frac{1}{\mathcal{V}} \int_{V_\beta} f \, dV, \qquad [25]$$

Accordingly, it follows from Eq. 23 and Eq. 25 that $\langle f \rangle = \varepsilon \langle f \rangle^\beta$.

In a similar way, we define the *interfacial surface average operator*

$$\langle f \rangle_{\beta\sigma} := \frac{1}{\mathcal{A}_{\beta\sigma}} \int_{A_{\beta\sigma}} f \, dA_{\beta\sigma}, \qquad [26]$$

where $\mathcal{A}_{\beta\sigma} = \int_{A_{\beta\sigma}} 1 \, dA_{\beta\sigma}$ is the interfacial surface area between phases β and σ within the unit cell, so that the electrode specific surface area is $a_v = \mathcal{A}_{\beta\sigma} / \mathcal{V}$.

Comprehensive derivations of the VAM are available in the literature (see e.g.[35,37,40]), therefore in the following we will focus on presenting the main results relevant for the current study.

Momentum conservation.—The electrolyte flow is governed by the incompressible Stokes equation, which can be written in nondimensional form as[40]

$$\nabla \langle p \rangle^\beta + \nabla \tilde{p} - \nabla^2 \mathbf{v} = 0, \quad \nabla \cdot \mathbf{v} = 0, \quad \mathbf{r} \in V_\beta, \qquad [27]$$

where the pressure field is decomposed as

$$p = \langle p \rangle^\beta + \tilde{p}. \qquad [28]$$

The pressure deviation field $\tilde{p}$ satisfies the periodic boundary condition

$$\tilde{p}(\mathbf{r} + \mathbf{l}_i) = \tilde{p}(\mathbf{r}), \quad \text{with} \quad \mathbf{l}_i = \mathbf{e}^{(i)} l_i, \qquad [29]$$

where $\mathbf{e}^{(i)}$ is the ith unit basis vector and l_i is the corresponding unit cell length. As a result, the volume-averaged dimensionless pressure gradient in Eq. 27, $\nabla \langle p \rangle^\beta$, is a unit vector (due to the selection of l_0 as the characteristic length) and its orientation dictates the direction of the electrolyte flow.

The electrolyte is assumed to have zero velocity at the fiber surfaces (no-slip condition) and the velocity field is periodic over the REV, that is

$$\mathbf{v}(\mathbf{r} + \mathbf{l}_i) = \mathbf{v}(\mathbf{r}). \qquad [30]$$

Upscaling of the Stokes equation with the VAM yields the well-known Darcy law, see e.g.[46], which can be expressed in nondimensional form as

$$\mathbf{K}_l \cdot \nabla \langle p \rangle^\beta = -\langle \mathbf{v} \rangle, \qquad [31]$$

where $\mathbf{K}_l$ is a symmetric and positive-definite permeability tensor, which is nondimensionalized with the characteristic scale $K_l^0 = (l^0)^2$.

First-order heterogeneous chemical reaction.—The application of the intrinsic volume averaging operator to the advection-diffusion equation coupled to a first-order heterogeneous chemical reaction and subsequent simplifications yields the macroscopic transport equation[37]

$$\varepsilon \text{Pe}_l^\star \nabla \cdot (\langle c_i \rangle^\beta \langle \mathbf{v} \rangle^\beta) = \varepsilon \nabla \cdot \left[\left(\nabla \langle c_i \rangle^\beta + \frac{a_{l,v}}{\varepsilon} \langle \mathbf{n}_{\beta\sigma} \tilde{c}_i \rangle_{\beta\sigma} \right) \right.$$
$$\left. - \text{Pe}_l^\star \langle \tilde{c}\tilde{\mathbf{v}} \rangle^\beta \right] - a_{l,v} \text{Ki}_l (\langle c_i \rangle^\beta + \langle \tilde{c}_i \rangle_{\beta\sigma}), \qquad [32]$$

where $a_{l,v}$ is the electrode specific surface area scaled with unit cell length. This transport equation is unclosed, since the deviation fields $\tilde{c}, \tilde{\mathbf{v}}$ are not known at the macroscale.

To derive a closed-form macroscopic transport equation, a closure ansatz is used for the deviation fields, e.g. for the concentration fields the ansatz

$$\tilde{c}_i = \mathbf{f} \cdot \nabla \langle c_i \rangle^\beta + g \langle c_i \rangle^\beta \qquad [33]$$

is inserted into the unclosed form of the transport equation, where $\mathbf{f}$ and g are unknown closure variables. As shown in[37] this results in the following periodic closure problems

$$\text{Pe}_l^\star (\tilde{\mathbf{v}} + \mathbf{v} \cdot \nabla \mathbf{f}) = \nabla^2 \mathbf{f} + \text{Ki}_l \langle \mathbf{f} \rangle_{\beta\sigma} \frac{a_{l,v}}{\varepsilon}, \quad r \in V_\beta, \qquad [34]$$

$$-\mathbf{n}_{\beta\sigma} \cdot \nabla \mathbf{f} = \text{Ki}_l \mathbf{f} + \mathbf{n}_{\beta\sigma}, \quad \mathbf{r} \in A_{\beta\sigma}, \qquad [35]$$

$$\mathbf{f}(\mathbf{r}) = \mathbf{f}(\mathbf{r} + \mathbf{l}_i) \quad \mathbf{r} \in V, \quad i = 1, 2, 3, \qquad [36]$$

$$\langle \mathbf{f} \rangle^\beta = 0, \qquad [37]$$

and

$$\text{Pe}_l^\star \mathbf{v} \cdot \nabla g = \nabla^2 g + \text{Ki}_l (1 + \langle g \rangle_{\beta\sigma}) \frac{a_{l,v}}{\varepsilon}, \quad \mathbf{r} \in V_\beta, \qquad [38]$$

$$-\mathbf{n}_{\beta\sigma} \cdot \nabla g = (g + 1) \text{Ki}_l, \quad \mathbf{r} \in A_{\beta\sigma}, \qquad [39]$$

$$g(\mathbf{r}) = g(\mathbf{r} + \mathbf{l}_i) \quad \mathbf{r} \in V, \quad i = 1, 2, 3 \qquad [40]$$

$$\langle g \rangle^\beta = 0. \qquad [41]$$

The closed equation now reads

$$\varepsilon \mathrm{Pe}_l^\star \nabla\cdot(\langle c_\alpha \rangle^\beta \langle \mathbf{v} \rangle^\beta) = \nabla\cdot(\varepsilon \mathbf{D}^* \cdot \nabla \langle c_\alpha \rangle^\beta)$$
$$- a_{l,v}\mathrm{Ki}_l^{\mathrm{eff}}\langle c_\alpha \rangle^\beta, \qquad [42]$$

where $\mathbf{D}^*$ and $\mathrm{Ki}^{\mathrm{eff}}$ are the dimensionless total dispersion tensor and the effective kinetic number, respectively, both of which depend on the closure variables $\mathbf{f}$ and g and are determined by

$$\mathbf{D}^* = \mathbf{I} + \frac{a_{l,v}}{\varepsilon}\langle \mathbf{n}_{\beta\sigma}\mathbf{f}\rangle_{\beta\sigma} - \mathrm{Pe}_l^\star\langle \mathbf{f}\tilde{\mathbf{v}}\rangle^\beta,$$
$$\mathrm{Ki}_l^{\mathrm{eff}} = \mathrm{Ki}_l(1 + \langle g\rangle_{\beta\sigma}), \qquad [43]$$

where $\mathbf{I}$ is the identity matrix. Note that the total dispersion tensor combines the effect of the heterogeneous reaction (second right-hand side term) and hydrodynamic dispersion (third right-hand side term) on mass transport, so that in the case of no convective flow (i.e. $\mathrm{Pe}_l^\star = 0$), the dispersion tensor reduces to the effective diffusion tensor, since

$$\mathbf{D}^* = \mathbf{D}^{\mathrm{eff}} - \mathrm{Pe}_l^\star\langle \mathbf{f}\tilde{\mathbf{v}}\rangle^\beta. \qquad [44]$$

Simplification of the reactive transport equations.—The transport equations for the electroactive species can be simplified by considering a change of variables from the individual species concentrations (c_{ox}, c_{red}) to the pair (c_T, c_{ox}), where c_T denotes the total species concentration $c_T = c_{\mathrm{ox}} + c_{\mathrm{red}}$, which satisfies the transport equation

$$\mathrm{Pe}_l^\star \mathbf{v}\cdot\nabla c_T = \nabla^2 c_T, \quad \mathbf{r} \in V_\beta, \qquad [45]$$

$$-\nabla c_T\cdot\mathbf{n}_{\beta\sigma} = 0, \ \mathbf{r} \in A_{\beta\sigma}, \qquad [46]$$

where we used the simplifying assumption of equal and constant diffusion coefficients of the electroactive species. Clearly, any constant function for the total species concentration c_T that satisfies the boundary conditions is a valid solution. This allows to reduce the transport problem to the equation

$$\mathrm{Pe}_l^\star \mathbf{v}\cdot\nabla c_{\mathrm{ox}} = \nabla^2 c_{\mathrm{ox}}, \quad \mathbf{r} \in V_\beta \qquad [47]$$

$$-\nabla c_{\mathrm{ox}}\cdot\mathbf{n}_{\beta\sigma} = -\mathrm{Ki}_l^{\mathrm{a}}\cdot(c_T - c_{\mathrm{ox}}) + \mathrm{Ki}_l^{\mathrm{c}}\cdot c_{\mathrm{ox}}, \quad \mathbf{r} \in A_{\beta\sigma}. \qquad [48]$$

The boundary condition of Eq. 48 can be written equivalently as

$$-\nabla c_{\mathrm{ox}}\cdot n_{\beta\sigma} = -k_0' + k_1' c_{\mathrm{ox}}, \quad r \in A_{\beta\sigma}, \qquad [49]$$

where $k_0' = \mathrm{Ki}_l^{\mathrm{a}} c_T$ and $k_1' = \mathrm{Ki}_l^{\mathrm{a}} + \mathrm{Ki}_l^{\mathrm{c}}$. Finally, using the variable transformation

$$c_{\mathrm{ox}} = c'_{\mathrm{ox}} + \frac{k'_0}{k'_1}, \quad c_T = c'_T, \qquad [50]$$

allows to write the transport equation with a linear reaction law as

$$\mathrm{Pe}_l^\star v\cdot\nabla c'_{\mathrm{ox}} = \nabla^2 c'_{\mathrm{ox}}, \quad x \in V_\beta, \qquad [51]$$

$$-\nabla c'_{\mathrm{ox}}\cdot n_{\beta\sigma} = k_1' c'_{\mathrm{ox}}, \ x \in A_{\beta\sigma}. \qquad [52]$$

This allows to reduce the problem of up-scaling the advection-diffusion equation coupled to a BV-type reaction law to the case of a linear reaction law.

The closed-form macroscopic transport equation immediately follows as

$$\mathrm{Pe}_l^\star \nabla\cdot(\varepsilon\langle v\rangle^\beta \langle c'_{\mathrm{ox}}\rangle^\beta) = \nabla\cdot(\varepsilon D^*\nabla\langle c'_{\mathrm{ox}}\rangle^\beta)$$
$$- a_{l,v}k_1'(1 + \langle g\rangle_{\beta\sigma})\langle c'_{\mathrm{ox}}\rangle^\beta, \qquad [53]$$

which can be stated in terms of the species concentration variable c_{ox} as

$$\mathrm{Pe}_l^\star \nabla\cdot(\varepsilon\langle \mathbf{v}\rangle^\beta \langle c_{\mathrm{ox}}\rangle^\beta) = \nabla\cdot(\varepsilon \mathbf{D}^*\nabla\langle c_{\mathrm{ox}}\rangle^\beta)$$
$$- a_{l,v}\mathrm{Ki}_l^{\mathrm{BV,eff}}(\langle c_{\mathrm{ox}}\rangle^\beta - \langle c_{\mathrm{ox}}^{\mathrm{eq}}\rangle^\beta), \qquad [54]$$

where we have introduced the effective kinetic number for the BV reaction at the interface

$$\mathrm{Ki}_l^{\mathrm{BV,eff}} = k_1'(1 + \langle g\rangle_{\beta\sigma}) = \mathrm{Ki}_l^{\mathrm{BV}}(1 + \langle g\rangle_{\beta\sigma}) \qquad [55]$$

with

$$\mathrm{Ki}_l^{\mathrm{BV}} = \mathrm{Ki}_l(e^{-\alpha\eta_{\mathrm{ref}}} + e^{(1-\alpha)\eta_{\mathrm{ref}}}) \qquad [56]$$

and the averaged equilibrium concentration

$$\langle c_{\mathrm{ox}}^{\mathrm{eq}}\rangle^\beta = \frac{k'_0}{k'_1} = c_T \frac{1}{1 + e^{-\eta_{\mathrm{ref}}}}, \qquad [57]$$

which is a function of the overpotential η_{ref}.

Alternative dimensionless scaling parameters.—Using the previously defined scaling parameters, we introduce the classical Reynolds and Péclet numbers

$$\mathrm{Re}_l = \frac{\rho l^0 |\langle \mathbf{v}\rangle|}{\mu} = |\langle \bar{\mathbf{v}}\rangle|\mathrm{Re}_l^\star,$$

$$\mathrm{Pe}_l = \frac{l^0 |\langle \mathbf{v}\rangle|}{D} = |\langle \bar{\mathbf{v}}\rangle|\mathrm{Pe}_l^\star \qquad [58]$$

defined with respect to the superficial average flow velocity, where we again employ *overline* symbols to differentiate nondimensional from dimensional quantities.

To facilitate the analysis and comparison of different pore-scale structures we additionally introduce dimensionless scaling parameters defined with respect to the fiber diameter d, which is considered fixed in this study.

The corresponding Reynolds, Péclet, and kinetic numbers defined with respect to d are given by

$$\mathrm{Re}_d = \mathrm{Re}_l\bar{d}, \quad \mathrm{Pe}_d = \mathrm{Pe}_l\bar{d}, \quad \mathrm{Ki}_d = \mathrm{Ki}_l\bar{d}, \qquad [59]$$

where $\bar{d} = d/l^0$ is the dimensionless fiber diameter. Other dimensionless quantities, such as the permeability tensor, are defined analogously, e.g. $\bar{\mathbf{K}}_d = \bar{\mathbf{K}}_l/\bar{d}^2$.

BV-type reaction in terms of a linear reaction law.—Since the upscaling of the BV-type reaction considered here can be expressed in terms of a linear reaction law, we present, if not stated otherwise, results based on the linear reaction law. The relation between the kinetic number of the linear reaction law and the parameters of the BV-type reaction can be expressed as

$$\mathrm{Ki}_d^{\mathrm{BV}} = \mathrm{Ki}_d(e^{-\alpha\eta_{\mathrm{ref}}} + e^{(1-\alpha)\eta_{\mathrm{ref}}}), \qquad [60]$$

where $\mathrm{Ki}_d^{\mathrm{BV}}$ is the kinetic number of the corresponding linear reaction law, which captures the dependency on the kinetic number and overpotential. Figure 3 displays the corresponding pairs of kinetic numbers and overpotentials (Ki_d, η_{ref}) for given values of $\mathrm{Ki}_d^{\mathrm{BV}}$ as isocontours.
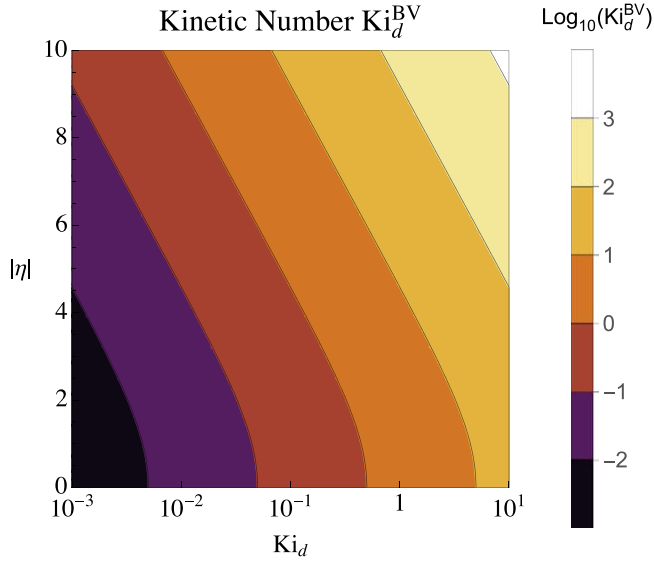
Figure 3. Isocontours of the reaction number Ki_d^{BV} in terms of the kinetic number Ki_d and the overpotential η, see Eq. 60.

Figure 5. Specific surface areas of the considered geometries.

Direct numerical simulation.—Complementary to the VAM approach, we perform a direct numerical simulation (DNS) to validate the VAM for a few given cases of the diffusion-advection-reaction equation. For a given geometry of the periodic unit cell, we create an array of N cells along the x-axis, as depicted in the lower panel of Fig. 4. Next, we resolve the pore-scale transport equations (Eq. 27, together with Eq. 17 and Eq. 19 for the first-order reaction or Eq. 52 for the BV-type reaction).

At the macroscopic inlet boundary we prescribe a fixed electrolyte concentration and impose a standard no diffusive flux BC at the

outlet, i.e. for species i we set

$$c_i = c_i^{in}(\mathbf{r}), \quad \mathbf{r} \in A_{\beta e}^{in}, \quad -\nabla c_i \cdot \mathbf{n}_{\beta e} = 0, \quad \mathbf{r} \in A_{\beta e}^{out}. \qquad [61]$$

Lastly, we impose symmetry BCs on the remaining upper and lower faces of the macroscopic domain according to

$$-\mathbf{n}_{\beta e} \cdot (Pe_l^{\star} \mathbf{v} - \nabla c_i) = 0, \quad \mathbf{r} \in \{A_{\beta e}^{up}, A_{\beta e}^{down}\}. \qquad [62]$$

Periodic unit cells.—To study the impact of different PE microstructures (e.g. fiber alignment or porosity) on the effective transport properties, we generate synthetic periodic PE geometries in 2D and 3D, which are juxtaposed in the upper panel of Fig. 4 for different porosity values.

The 2D geometries include the simple cubic (SC) and hexagonal (H) geometries composed of fibers with disc (d) and square (s) cross-sections. The 3D geometries include the mono-fiber SC in cross-flow
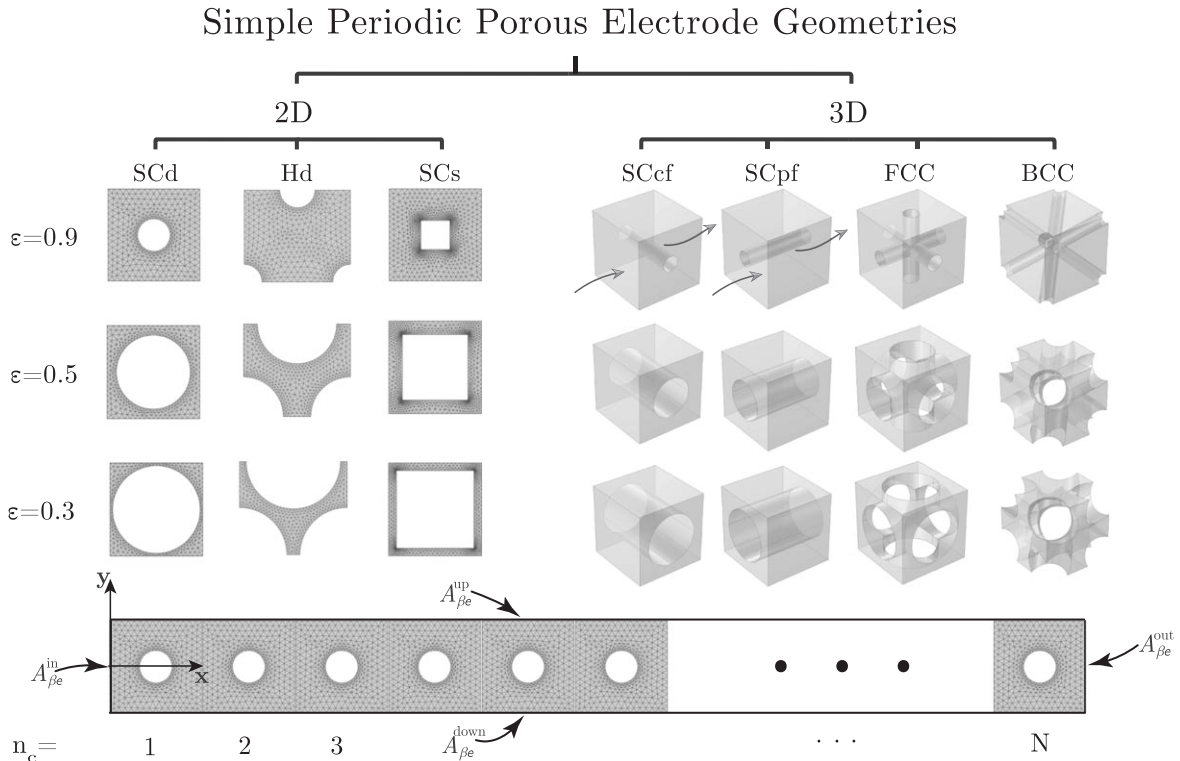

Figure 4. Upper panel: Simple periodic porous electrode geometries considered in this study in 2D and 3D: SC = simple cubic, H = hexagonal, FCC = face-centered cubic, BCC = body-centered cubic; d = fibers with disc cross-section, s = fibers with square cross-section (for literature study validation only), cf = cross-flow, pf = parallel flow. Lower panel: a PE geometry consisting of N SCd single cells for a DNS. Gray volume symbolizes voids filled with electrolyte.

Table I. Comparison of standard heterogeneous reaction rate constants, diffusion coefficients, and the resulting kinetic numbers for a number of different redox active species commonly used in flow batteries. Estimations of Ki$_l$ are based on $l^0 = 30\,\mu$m. Typical values for common redox pairs in electrochemistry are given for reference.

Flow battery system	Redox-active species	$k/(cm\ s^{-1})$	$D_i/(10^{-6} cm^2\ s^{-1})$	Ki$_l$/(-)	Electrode	Comments	Source
Vanadium	VO^{2+}/VO_2^+	$1.35 \cdot 10^{-5}$	2.26	0.018	Planar glassy carbon	in 2 M H_2SO_4	50
Bromine-based	Br_2/Br^-	$5.80 \cdot 10^{-4}$	1.60	0.109	Vitreous carbon	Mean diffusion coefficient of bromine and bromide in water 51	49
Aqueous organic, acidic	Anthraquinone-2,7-disulfonic acid (2,7 AQDS)	$7.20 \cdot 10^{-3}$	3.80	5.68	Glassy carbon	in 1 M H_2SO_4	52
Aqueous organic, alkaline	1,8-Dihydroxyanthraquinone (1,8-DHAQ)	$1.690 \cdot 10^{-2}$	8.43	6.01	Glassy carbon	in 1 M KOH	53
Aqueous organic, neutral	4-HO-TEMPO	$5.13 \cdot 10^{-2}$	19.1	8.06	Glassy carbon	in 1 M KCl	54
—	$Ru(NH_3)_6^{3+}/Ru(NH_3)_6^{2+}$	0.8	7.90	303	Pt	in 1 M KCl	55
—	$Fe(CN)_6^{4-}/Fe(CN)_6^{3-}$	0.14	6.30	66.7	Pt	in 1 M NaCl	55
Lower bound of k° in practical FB	—	$1.00 \cdot 10^{-5}$	1.00	0.03	—	the typical diffusion coefficient of redox species in electrolyte solutions	49

(cf) and parallel-flow (pf) arrangements, face-centred cubic (FCC) and body-centred cubic (BCC) geometries, all of which have disc cross-sections.

The SCs geometry is only used to validate the result with the available data in the literature. For all other studies, we employ the disc cross-section as the square is rather unlikely to correspond to an actual carbon fiber shape in the PE for FB applications.

The specific surface area of PEs that are either composed of spherical particles with mean sphere diameter d or cylindrical filaments of diameter d can be stated in analytical form as[13]

$$a_{d,v} = b(1 - \varepsilon),\qquad [63]$$

where $b = 6$ for spherical particles and $b = 4$ for cylindrical filaments[47] and $a_{d,v} = a_{l,v}\bar{d}$ is the dimensionless specific surface area scaled with the fiber diameter. In Fig. 5 we show the specific surface areas $a_{d,v}$ of the considered geometries, where $a_{d,v}$ coincides with Eq. 63 for the SCd, SCh, and SCpf geometries. However, for the FCC and BCC structures the specific surface area is reduced, which is due to the overlapping region of the fibers.

Dimensionless numbers in FB systems.—Electrochemistry deals with reaction constants k ranging over more than ten orders of magnitude. Single electron transfer reactions of $\mathcal{O}(k) = 10$ cm s^{-1} without molecular structure reorganisation have been reported and can be regarded as relatively fast.[48] On the other hand, sluggish reactions with $\mathcal{O}(k) = 10^{-9}$ cm s^{-1} are not uncommon in electrochemistry.[48]

In most FB applications, k does not need to be extremely high, as the reaction rate is enhanced electrochemically by applying sufficiently large overpotentials.[48] However, k should also not be too low to prevent excessive activation polarization and irreversibility of the redox reactions.

Based on given requirements of a FB system, such as high round-trip efficiency, cell voltage, specific surface area, electrolyte concentration, and conversion rate of electro-active species, Weber et al.[49] proposed a value $k = 10^{-5}$ cm s^{-1} as the minimum rate constant for practical FB applications.

In Table I we show reported values of the reaction rate, diffusion coefficient and the dimensionless kinetic number Ki$_d$ for a range of different FB systems. The listed values indicate that the reported redox-active organic molecules have a kinetic number in the range of

$1 < $ Ki$_d < 10$, while e.g. the kinetic rates of the inorganic vanadium and bromine-based species are significantly smaller satisfying Ki$_d < 0.1$.

FBs with relatively slow electrode kinetics such as VFBs require higher operating overpotentials in order to maintain high electrochemical reaction rates. From[56] (Fig. 2 therein) we estimate a typical activation loss in VFB system to be in the order of 350 mV, which at 298.15 K yields the dimensionless overpotential of $\eta = 13.6$. For other systems with faster kinetics the maximum expected η will be lower.

To estimate the ranges of Péclet numbers Pe$_d$ encountered in actual FB applications, we explored the available literature on (preferably experimental) FB studies. Milshtein [57] used a symmetric iron FB cell with carbon paper as the PE (25AA from SGL, assuming $\varepsilon = 0.75$). The cell operated at flow rates from 0.5 up to 10 mL min^{-1} (superficial velocity was estimated from the volumetric flow rate and electrode width and height). Milshtein et al. assumed a typical diffusion coefficient of ions in aqueous solution of $5 \cdot 10^{-6}$ cm^2 s^{-1}, which yields the range of Péclet numbers $51 < $ Pe$_d < 1057$ for the characteristic fiber diameter $d = 1 \times 10^{-5}$ m used in this work.

Finally, it is crucial to determine whether the electrolyte flow inside a real FB can be modeled as creeping in order for Eq. 27 to hold. Xu et al.[58] studied flow through disordered and ordered 2D media with square pore cross-section using the LBM. By analysing the dependence of hydraulic permeability, **K**, on Re$_d$ (with the characteristic length d defined as the side length of the square fiber and the velocity being intrinsic), Xu et al. determined the critical Re$_d$ at which **K** is not any more independent of Re$_d$, indicating the onset of the inertial regime. Based on the simulation results of Xu et al. (Fig. 6 therein) the critical Re$_d$ depends significantly on both ε (critical Re$_d$ increasing with decreasing ε) and the fiber alignment. However, the condition Re$_d < 1$ in general ensures that inertial effects are insignificant, which for Sc $= 1000$ is satisfied when Pe$_d < 1000$, since Pe$_d = $ Re$_d$ Sc.

Lastly, to estimate the practical ranges of ε for our simulations, we refer to the study by Zenyuk et al.[59] to conclude that the porosity of various carbon materials in FB applications normally spans between $\varepsilon = 0.6$ and $\varepsilon = 0.9$, depending strongly upon compression.

The above estimations serve as a basis for selecting ranges of the values of dimensionless numbers in parameter studies presented in the next section.
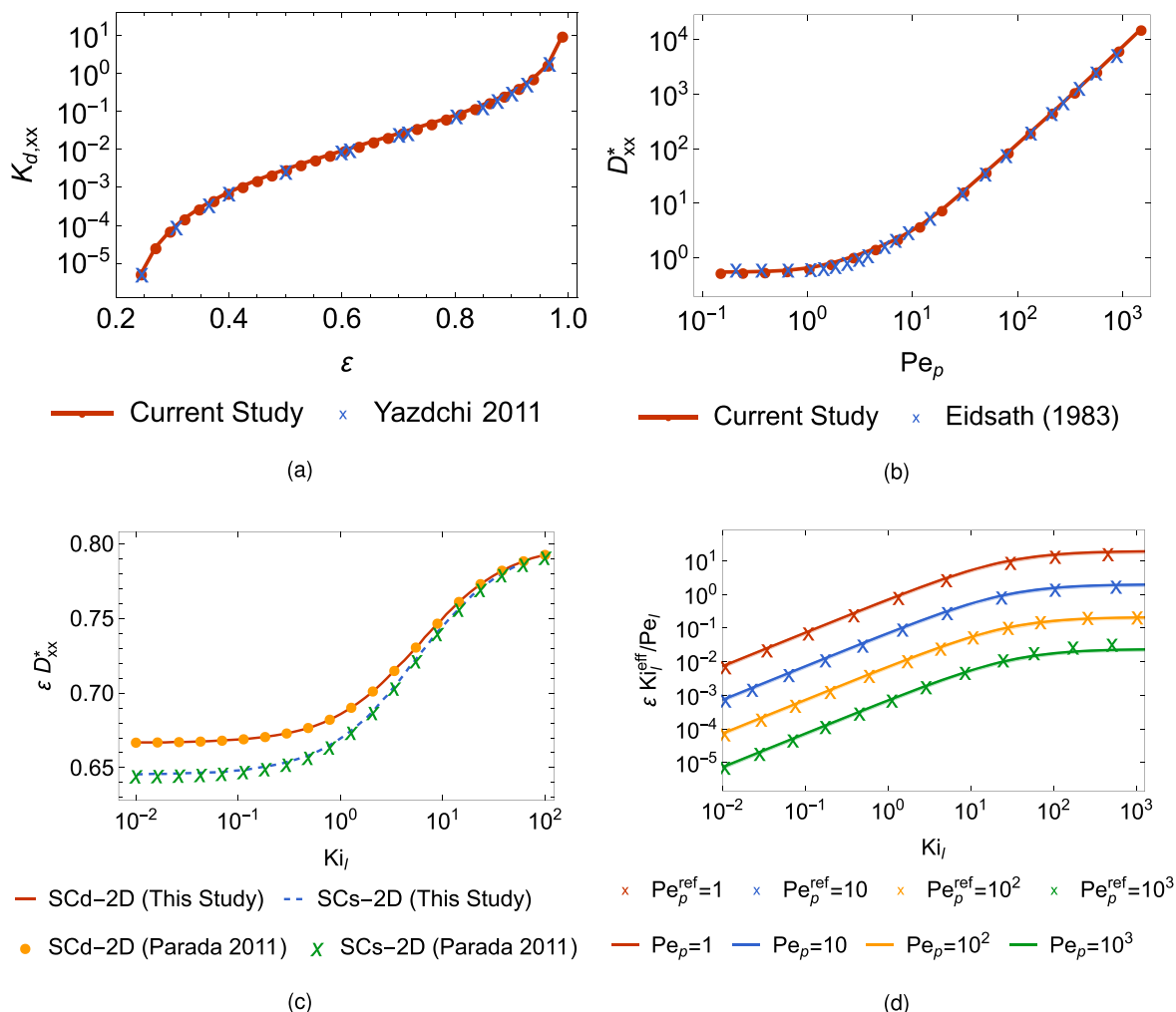
Figure 6. Verification studies of the VAM-based results showing (a) simulated dimensionless permeability $K_{d,xx}$ vs ε and a comparison with reference data from;[60] (b) simulated dimensionless effective diffusivity D^*_{xx} vs Pe_p and a comparison with reference data from;[61] (c) simulated dimensionless total dispersion D^*_{xx} vs Ki_l; and (d) simulated dimensionless effective kinetic number vs Ki_l and a comparison with reference data from.[37]

Results and Discussion

In this section we present numerical studies of the effective parameters determined by the VAM-based approach described previously. As we are interested in studying the effects of convection, diffusion and reaction on the macroscopic effective parameters, we focus here for simplicity on 1D flow problems over domains along the *x*-axis. This allows a reduction of the permeability, diffusion, and dispersion tensors to the scalar variables $K_{d,xx}$, D^{eff}_{xx}, and D^*_{xx}, respectively.

Model verification with literature data.—To verify our implemented VAM-based upscaling method, we present the relevant effective parameters for a range of operating conditions against published results in Fig. 6.

Permeability.—First, we simulate electrolyte flow in a periodic SCd geometry. We set $Re^\star_l = 10^{-4}$ and determine the xx-component of the dimensionless permeability tensor, K_{xx}. We then compare K_{xx} with the results provided in[60] (Fig. 2a therein), and plot them in Fig. 6a.

We conclude that the results of the current study are in excellent agreement with the reference data, which allows us to simulate the Stokes flow in other periodic geometries with confidence.

Total dispersion in a non-reactive system.—Next, we consider a system in which no reaction is taking place at the electrode surfaces and the fluid is allowed to flow ($Re^\star_l \in [0.2, 2000]$) and diffuse in the SCd spatially periodic geometry ($\varepsilon = 0.37$). We then evaluate D^*_{xx} from the VAM and compare with the corresponding results obtained in[61] (Fig. 12 therein), which is depicted in Fig. 6b. Following the reference source,[61] we plot the total dispersion against the particle Péclet number, defined as

$$Pe_p = 6\frac{Pe_d}{a_{d,v}}. \qquad [64]$$

Overall, we observe an excellent agreement with the literature reference over a very broad range of Pe_p. While in the limiting case of no convective flow $Pe_p \to 0$ the dispersion coefficient converges to the effective diffusion, we observe a quadratic increase in D^*_{xx} for large Péclet numbers, which coincides with the Taylor-Aris dispersion relation, see e.g.[62]

Total dispersion: diffusion and 1st order reaction.—To simulate a reactive system without macroscopic flow and a 1st-order chemical reaction assumed at the fiber surfaces, we impose a no convective flow condition by setting $Re^\star_l = 10^{-12}$ and sweep the kinetic number over the range $Ki_l \in [0.01, 100]$ for the SCd and SCs geometries
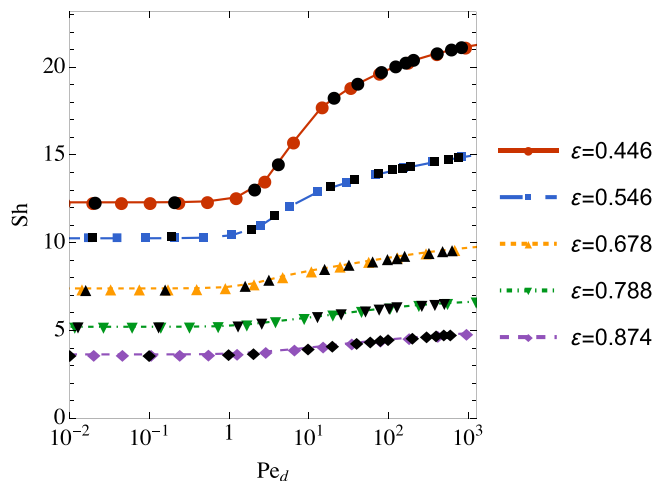
Figure 7. Variation of Sh with Pe_d for SCd geometry for different porosities and a comparison to published results,[63] Fig. 7c therein (black symbols). Lines connecting the points serve as a guide to the eye only.

with $\varepsilon = 0.8$. The resulting total dispersion multiplied by ε, together with the reference data[37] (Fig. 4a therein), is shown in Fig. 6c.

In the limit of small reaction rates, $Ki_l \to 0$, the effective diffusion converges to a constant that depends only on the pore-scale geometry. On the other hand, in the limit of dominating reactions, $Ki_l \to \infty$, the effective diffusion converges toward the molecular diffusion.[37]

Total dispersion.—We then simulate the coupled system with convection, diffusion and a 1st-order heterogeneous reaction. For this, we perform a parameter sweep over $Ki_l \in [0.01, 1000]$ and $Re_l^\star \in [1.6, 1900]$, which corresponds to Pe_p values between 1 and 1000, and set $\varepsilon = 0.37$ for the SCs geometry. We present the results of an evaluated ratio Ki_l^{eff}, together with the reference data from[37] (Fig. 9 therein), in Fig. 6d.

The effective reaction rate can be observed to increase linearly for small kinetic numbers until a plateau is reached in the limit of large kinetic numbers for all values of Pe_l, due to diffusional transport limitations. While slight discrepancies at high kinetic rates ($Ki_l > 100$) and particle Péclet numbers ($Pe_p > 100$) can be observed, which may be caused by different numerical discretisation errors, the results of this study agree well with the published data.

Sherwood number.—Hamid and Smith[63] used a similar upscaling strategy to derive the effective mass transport in porous electrodes, for which they assumed facile electrochemical kinetics, which corresponds to the limiting case of large kinetic numbers.
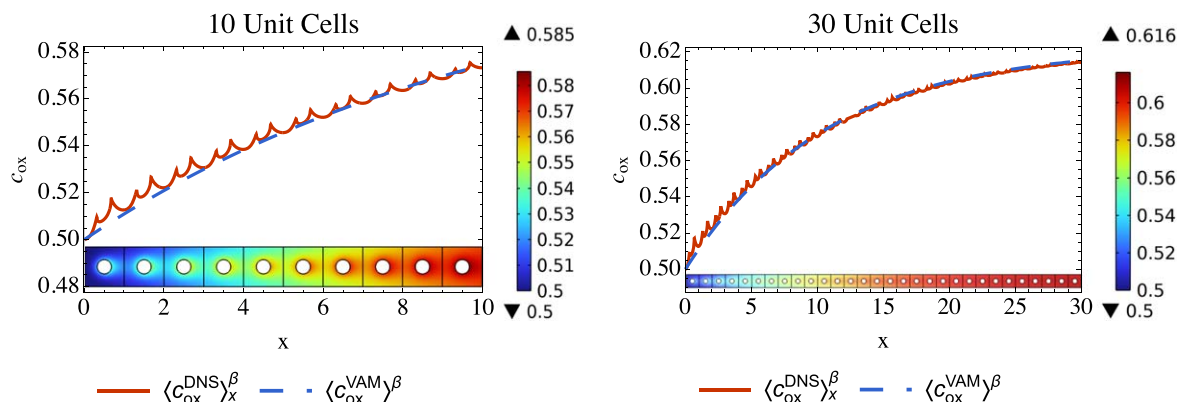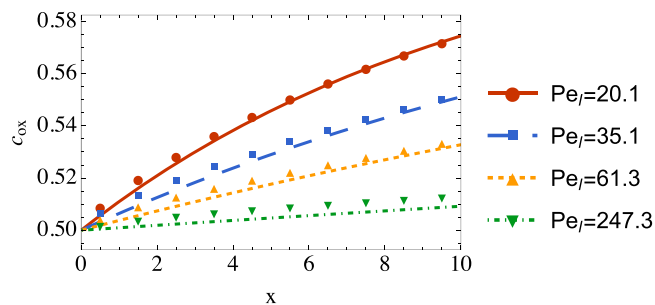

Figure 9. Comparison of VAM and DNS approaches for different Pe_l (other parameters remain the same as in Fig. 8). The lines represent $\langle c_{ox}^{VAM} \rangle^\beta$, while the symbols represent the per-cell average, $\langle c_{ox}^{DNS} \rangle^\beta$.

The Sherwood number, defined as $Sh = k_m d/D$, where k_m is the mass transfer coefficient ($m\,s^{-1}$), is the ratio of the diffusion timescale d^2/D to the mass transport timescale d/k_m, indicating the importance of the mass transport with respect to diffusive transport. In the limiting case of large current densities we find that the Sherwood number is directly related to the effective kinetic number by $Sh = Ki_d^{eff}$. Figure 7 shows the Sherwood number over a large range of Péclet numbers for the SCd geometry and several porosity values, where we used a high kinetic number of $Ki_d = 1000$ to approximate the limiting case studied in[63] illustrated as black symbols in the plot.

We conclude that the agreement with the reference data is excellent. Hamid and Smith noticed effects relevant for our further study: from the mass transport perspective alone, due to the redistribution of the diffusive flux at $1 < Pe_d < 15$ and a dramatic increase of Sh, low porosity media are preferred in flow cells applications. However, low porosity media suffer from low hydraulic permeability, increasing pumping losses. We will reconsider these competing effects in an optimisation study further below.

Validation of the VAM against the DNS.—To investigate the validity and accuracy of the VAM approach we compare the resulting macroscopic solution with fully-resolved DNS results. For this we consider the solution to the reactive mass transport problem over a one-dimensional domain shown in Fig. 2.

For the considered transport problem we set the inflow concentration $c_{ox}^{(in)} = 0.5$, the Péclet number $Pe_l = 20.1$, and employ the BV-type reaction with kinetic number $Ki_l = 1$ and overpotential $\eta_{ref} = 0.5$. The pore-scale geometry is SCd with porosity $\varepsilon = 0.9$.

In Fig. 8 we show the intrinsic average species concentration of c_{ox} of the upscaled macroscopic transport equation, together with the projected DNS solution $\langle c_{ox}^{DNS} \rangle_x^\beta$, which is evaluated by averaging the concentration of c_{ox} over the y-axis as

Figure 8. Intrinsic concentration averages of the VAM-approach and the DNS result over 10 and 30 repeated unit cells.
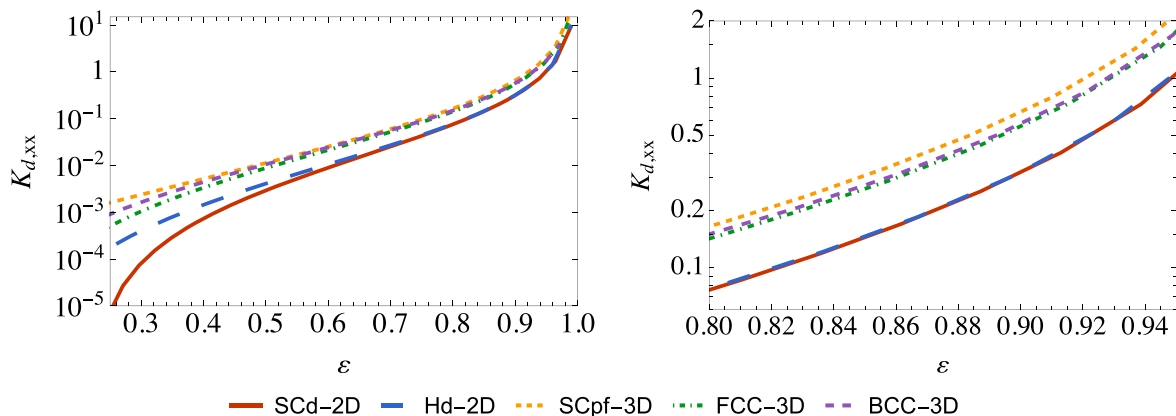
Figure 10. Dimensionless hydraulic permeability $K_{d,xx}$ of porous electrodes composed of different simple periodic structures as a function of porosity.

$$\langle c_{ox}^{DNS} \rangle_x^\beta = \frac{1}{\mathcal{V}_{\beta x}} \int_{V_{\beta x}} c_{ox}^{DNS}(x, y) dy \quad \text{with}$$

$$V_{\beta x}(x) = V_\beta \cap \{\mathbf{x} | \mathbf{x} \cdot \mathbf{e}^{(1)} = x\}, \quad \mathcal{V}_{\beta x} = |V_{\beta x}|. \quad [65]$$

Assuming a fiber diameter of $10\,\mu m$, the corresponding dimensional unit cell length is $28\,\mu m$, so that the overall domain lengths for $N = 10$ and $N = 30$ unit cells are $280\,\mu m$ and $841\,\mu m$, respectively.

The reference DNS reveals repetitive fluctuations of the species concentration over the unit cells due to the production of oxidized species at the electrode surface. Clearly, the resolution of these concentration fluctuations becomes infeasible over large macroscopic domains. On the other hand, the upscaled macroscopic transport equation does not show any fluctuations as expected, but follows the DNS in an averaged sense.

It is also desirable to verify the applicability of the VAM method at different flow velocities. Hence, we keep the same parameters and geometry (for $N = 10$) and repeat the simulation for various Pe_l values, as shown in Fig. 9.

A comparison of the VAM solution (lines) with the cell-averaged DNS solution (symbols) reveals a good agreement for smaller Péclet numbers. The visible discrepancy for larger Péclet numbers is expected as the solution to high Péclet number flows through porous materials can depend strongly on the macroscopic boundary condition. As the VAM assumes a local spatially periodic solution

independent of macroscopic boundary conditions, it fails in representing such transport problems accurately close to the macroscopic boundary.

Numerical study of the effective parameters.—In this section, we present additional numerical studies of the effective parameters over transport parameter ranges relevant for FB applications.

Hydraulic permeability.—Pressure drop is one of the key characteristics of FB systems as it is directly related to the parasitic losses due to the energy spent on pumping. Our model is capable of predicting the hydraulic permeability of the PE given the periodic unit cell geometry and porosity. In Fig. 10 we present the xx-component of the dimensionless hydraulic permeability tensor for all studied periodic geometries as a function of porosity, setting $\text{Re}_l^\star = 10^{-4}$.

The problem of predicting the permeability, for a given pore-scale structure, has been discussed to a great extent in the literature.[40,46,60,64–67] In general, the largest relative difference in the permeability occurs at small porosities (e.g. below 0.5).

The evaluated permeabilities for the different structures fall in the same range of values determined by Kok et al.[28] for a carbon felt material, where permeability values in the range $K_{d,xx} \in [0.33, 0.58]$ were computed for estimated porosity values $\varepsilon \in [0.87, 0.93]$.

Effective diffusion and dispersion.—The total dispersion tensor in PEs is affected by four factors: (1) the intrinsic, molecular diffusion
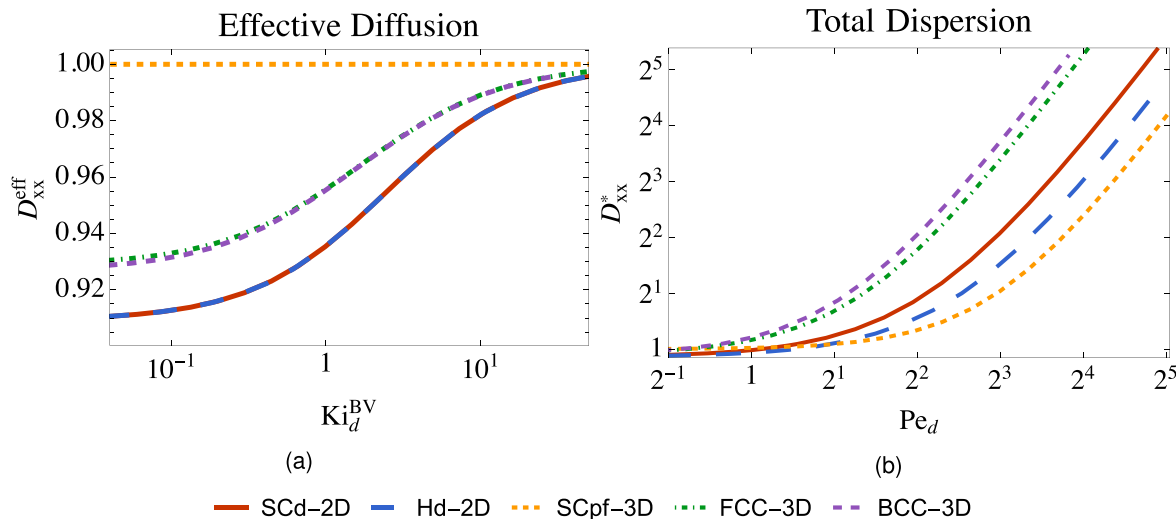

Figure 11. (a) Effective diffusion as a function of Ki_d in the passive diffusion case and (b) the total dispersion along the x-axis as a function of Pe_d for several simplified periodic geometries (for other constant parameters cf. text).
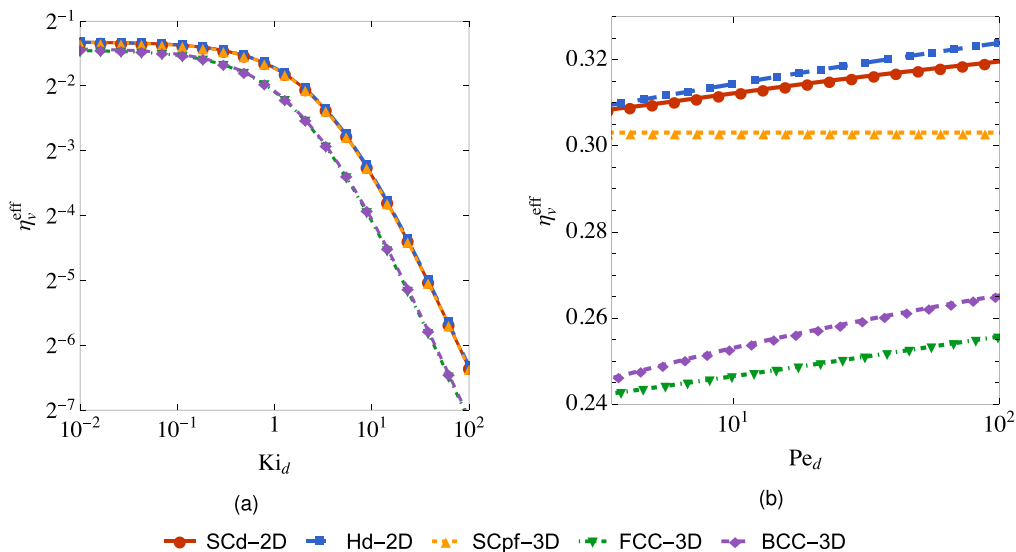
Figure 12. Volumetric effectiveness factor as a function of Ki_d for the passive diffusion case (a) and with convection (b).

coefficient, (2) the meso-structure geometry, (3) the convective mass transport in the electrode as well as (4) the reactions in the PE.

In Fig. 11a we show the dependency of the effective dispersion coefficient D_{xx}^{eff} on Ki_d for a passive diffusion transport ($Pe_d = 0$) using different geometries at constant $\varepsilon = 0.9$. For the flow-aligned fiber structure SCpf we find that the electrochemical reaction has no effect on the diffusion as $D_{xx}^{eff} = 1$, since the flow-aligned structure allows species to diffuse unhindered in straight paths along the x-direction, so that the effective diffusion rate equals the molecular diffusion. For all other investigated structures, we observe a reduced effective diffusion rate due to the blockage of the species transport by the fibers, which leads to longer effective diffusion paths.

In Fig. 11b we show the total dispersion D_{xx}^* as a function of Pe_d for all considered geometries with constant $\varepsilon = 0.9$ and a small kinetic number $Ki_d = 0.1$. We observe that the dispersion increases quadratically in Pe_d for all considered unit cells. Furthermore, we note a significant variation in the dispersion between the studied structures, where the flow-aligned structure shows the smallest dispersion, while the more complex FCC and BCC structures exhibit the highest dispersion.

Volumetric effectiveness factor.—To quantify PE structures in terms of the combined effect of the provided specific surface area and the effectiveness of the mass transfer to the electrode surface, we introduce the volumetric effectiveness factor

$$\eta_v^{eff} = a_{d,v}(1 + \langle g \rangle_{\beta\sigma}). \quad [66]$$

The volumetric effectiveness factor can be interpreted as representing an effective specific surface area in direct contact with the reactant species at its bulk concentration, so that the electrochemical reaction is only limited by reaction kinetics.

Clearly, η_v^{eff} depends directly on the pore-scale geometry through the term $a_{d,v}$. Additionally, it is also indirectly affected by the operating conditions, such as the Péclet number Pe_d and the applied overpotential η, through the scalar closure variable g, defined in Eq. 33.

The volumetric effectiveness factor η_v^{eff} is shown in Fig. 12a as a function of the kinetic number Ki_d for the passive diffusion scenario ($Pe_d = 0$). In the limit of small kinetic numbers $Ki_d \to 0$ we find $\langle g \rangle_{\beta\sigma} \to 0$, so that the volumetric effectiveness factor tends toward the specific surface area $a_{d,v}$. On the other hand, in the limit of large
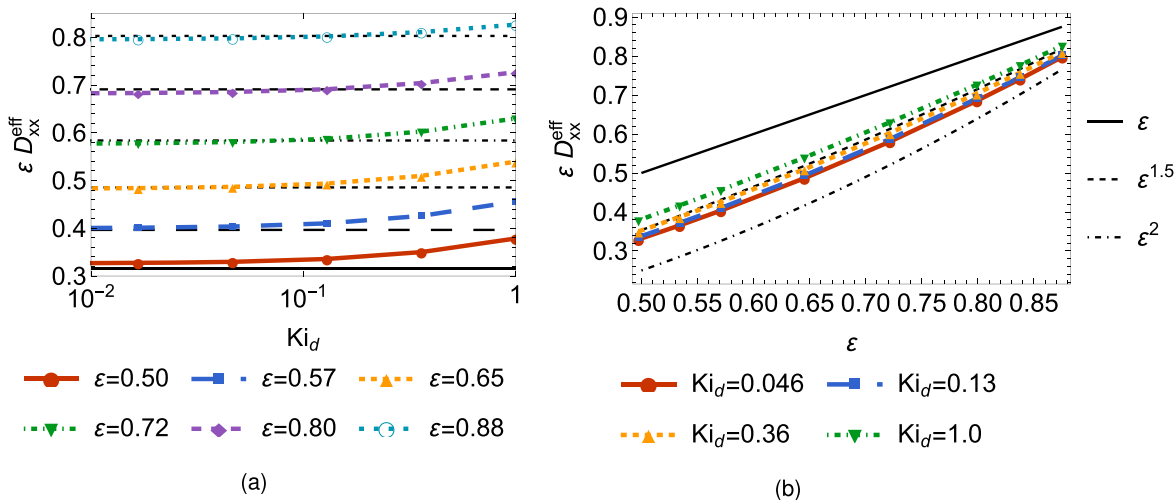

Figure 13. (a) Simulated effective diffusivity (VAM) as a function of Ki_d without convective flow for different porosities and compared with the Bruggeman relation of $D_{xx}^{eff} = D\varepsilon^{1.65}$ (black, broken lines); (b) Simulated effective diffusivity as a function of porosity for several values of Ki_d compared with three different power laws, including the Bruggeman correction for non-overlapping, randomly placed cylinders. Both Figs. generated using the BCC geometry.
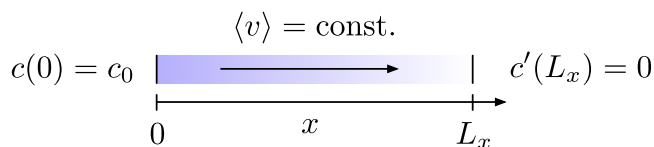
Figure 14. Illustration of macroscopic 1D porous electrode domain.

kinetic numbers, the volumetric effectiveness factor tends to zero, as the overall reaction rate becomes limited by the diffusive transport. We note a clustering of the results in two groups: The SCd, Hd, and SCpf structures show a very similar effectiveness factor and perform significantly better in comparison to the FCC and BCC structures. This difference can be explained by a lower specific surface area of the FCC and BCC structures.

Figure 12b displays the relative increase of η_v^{eff} due to convective flow over a range of Péclet numbers, for a constant $\mathrm{Ki}_d = 1$. While the effectiveness factor does not increase at higher Péclet numbers for the flow-aligned fiber structure SCpf, all other investigated structures display an increase in the effectiveness factor, which is most pronounced for the BCC structure.

Comparison of the VAM with the Bruggeman correction.— Next, we simulate a mass transport problem in the BCC geometry with no convective flow. From the VAM, we calculate the total dispersion and compare with the predictions of the effective diffusion coefficient from Eq. 1 and Eq. 2, which is a common ansatz utilized in the FB modeling literature. Figure 13a shows the effective dispersion coefficient for a range of electrode porosities and kinetic numbers Ki_d. For each simulated curve (colored lines), we provide the corresponding prediction of the effective diffusion coefficient from the Bruggeman model with $D_{xx}^{\mathrm{eff}} = D\varepsilon^{1.65}$ (black horizontal lines). The effective diffusion predicted by VAM shows a non-linear behavior across the whole range of Ki_d and ε. This contrasts with the Bruggeman model, which only considers the impact of porosity on the effective diffusion.

In the limiting case of small kinetic numbers ($\varepsilon \to 0$), the effective diffusion is determined by the tortuosity. Here we find a good agreement of the predicted effective diffusivity and the Bruggeman-type relation $D_{xx}^{\mathrm{eff}} = D\varepsilon^{1.65}$. However, as the kinetic number increases, the Bruggeman relation largely underestimates the effective diffusion tensor. This is due to the fact that the Bruggeman correction does not account for the coupled effect of diffusion and heterogeneous reactions.

Next, in Fig. 13b, we show D_{xx}^{eff} plotted over a range of ε values for four different values of Ki_d and compare with Eq. 2 for three different exponent values which are used to correct the diffusion coefficient.

For these particular conditions, we find that the typically used Bruggeman relation $D_{xx}^{\mathrm{eff}} = D\varepsilon^{1.5}$ for the effective diffusion to well approximate a reaction with $\mathrm{Ki}_d \approx 0.36$. However, depending on the Ki_d value, the Bruggeman relation either over- or underestimates the result of VAM, which shows the shortcoming of the former.

Furthermore, the effect of convective flow (dispersion) on D_{xx}^{eff} is also not included in the Bruggeman relation Eq. 1. However, this effect is not negligible for $\mathrm{Pe}_d > 1$, as shown previously in Fig. 11b and is not captured by standard macrohomogeneous FB models.

In general, we find that using the VAM method allows evaluating the effective total dispersion parameter, which is sensitive to geometry, macroscopic flow conditions (dispersion), and heterogeneous reaction. Such dependency is a major weakness of the modeling approaches utilising the Bruggeman relation.[8,9]

Optimisation study of the pore-scale structure.—Let us apply the up-scaling methodology to the problem of determining optimal pore-scale geometries that maximize the overall efficiency of a porous electrode. For this we consider the simplified macroscopic one-dimensional porous electrode illustrated in Fig. 14, where the electrolyte concentrations of the electroactive species at the inlet boundary is given by Dirichlet boundary conditions and simple natural Neumann boundary conditions are imposed on the outlet boundary.

With the abbreviations $c \equiv \langle c \rangle^\beta$, $c^{\mathrm{eq}} \equiv \langle c^{\mathrm{eq}} \rangle^\beta$, the one-dimensional mass balance equation can be expressed as

$$\mathrm{Pe}_M c' = \varepsilon c'' - a_{d,v} \mathrm{Ki}_M^{\mathrm{BV,eff}}(c - c^{\mathrm{eq}}),$$
$$c(0) = c_0, \quad c'(L_x) = 0, \qquad [67]$$

where $\mathrm{Pe}_M = \mathrm{Pe}_d / D^*$ and $\mathrm{Ki}_M^{\mathrm{BV,eff}} = \mathrm{Ki}_d^{\mathrm{BV,eff}} / D^*$ denote the Péclet and kinetic numbers scaled with respect to the effective macroscopic total dispersion.

For the above one-dimensional transport problem, the specific energy dissipation rate[68] (defined as the dissipation rate of energy per mass of fluid flowing in the porous medium) can be stated in non-dimensional form by

$$\eta^{\mathrm{diss}} = \frac{\langle v \rangle^2}{\varepsilon K_{d,xx}}. \qquad [68]$$

The analytical solution to Eq. 67 allows for a closed-form expression of the spatially averaged reaction rate

$$\langle s \rangle = a_{d,v} \mathrm{Ki}_d^{\mathrm{BV,eff}} \frac{1}{L_x} \int_0^{L_x} (c(x) - c^{\mathrm{eq}}) \mathrm{dx}. \qquad [69]$$
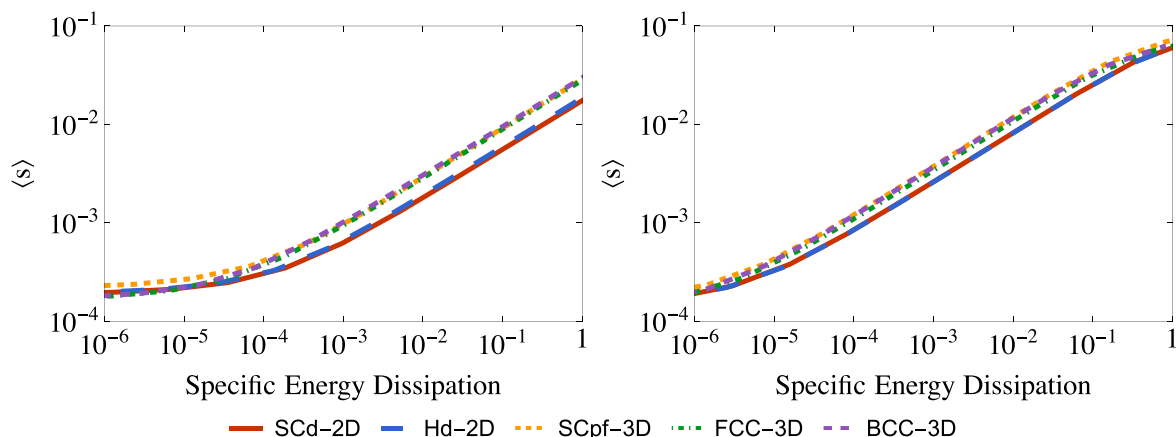

Figure 15. Average reaction rate over a range of specific energy dissipation values for the considered pore-scale structures with $\varepsilon = 0.6$ (left) and $\varepsilon = 0.85$ (right).
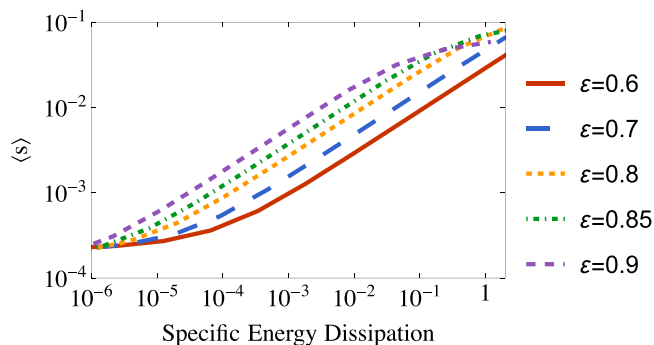
Figure 16. Average reaction rate over a range of specific energy dissipation values for the SCpf geometry with different porosity values.

In the following we set the macroscopic domain size to $L_x = 10^3$, which corresponds to a length of 1 cm. Additionally, we set the dimensionless inflow concentration of the reactant to $c_0 = 0.5$ with an equilibrium concentration of $c^{eq} = 1/(1 + \exp(-\eta_{ref}))$, where $\eta_{ref} = -1$, and a kinetic reaction number of $Ki_d = 0.44$.

Figure 15 displays the averaged reaction rate over a wide range of specific energy dissipation values for the considered pore-scale geometries at a fixed porosity values of $\varepsilon = 0.6$ (left) and $\varepsilon = 0.85$ (right). We find that the averaged reaction rates level off in the limit of small specific energy dissipations. In this limit the Péclet number converges to zero, so that the transport becomes fully diffusion-driven.

Ordering the structures from highest to lowest average reaction rate yields

$$SCpf > Hd \approx SCd > FCC > BCC \qquad [70]$$

for small specific dissipation energy values, whereas the ordering changes to

$$BCC \approx SCpf \approx FCC > Hd > SCd \qquad [71]$$

at high values of η^{diss}. These changes can be explained by the different permeability values of the structures: While the cross-flow aligned Hd and SCd structures allow for a high reaction rate compared to the FCC and BCC at low dissipation rates, their comparatively lower permeability leads to increased energy dissipation rates at high flow velocities, where both the FCC and BCC become favourable. Overall, the flow-aligned fiber structure SCpf shows very good performance.

To investigate the impact of the porosity on the reaction rate, we show in Fig. 16 the performance of the flow-aligned structure SCpf

for different porosity values. The results indicate that higher porosity values are favourable at lower specific energy dissipation values, whereas lower porosity values allow for an increased average reaction rate at higher dissipation rates thanks to their increased specific surface areas.

Surrogate model.—In this work we have assumed the pore-scale geometry and transport conditions to be spatially homogeneous. However, the results presented here can also be applied to inhomogeneous materials or transport problems with spatially (or temporally) varying conditions, given that material property gradients occur over macroscopic length scales much larger compared to a single unit cell, see.[35]

When simulating transport problems through porous electrodes with variable material properties, such as spatially inhomogeneous porosity values in graded materials, there is a need for repeated evaluation of the effective parameters. To avoid the necessity for multiple numerical solutions for the effective parameters when solving the macroscopic PDE, we propose a two-step approach: First, the effective parameters are solved for a set of parameter values that are sampled over a parameter space. For each effective parameter a surrogate model is constructed using the evaluated effective transport coefficients at the sampled parameters. Second, the surrogate model is used to evaluate the required effective parameters when solving the macroscopic transport equation.

Here we use the Kriging approach to provide a fast evaluation of the effective parameters, see e.g.[69,70] The Kriging estimator interpolates the given sample values and provides an estimation at the unsampled points based on a weighted average of the sampled values located in a neighbourhood, together with an estimate of the uncertainty. To generate and evaluate the Kriging model, we make use of the *Surrogates.jl* Julia package.[71] For the effective parameters Ki_d^{eff} and D_{xx}^* we generated a Kriging model from $N = 10^3$ samples over the parameter space (ε, Pe_d, Ki_d). An open-source implementation of this procedure is maintained in a Github repository.[72]

Figure 17 shows the predictions of the surrogate model for the effective dispersion and kinetic number (contour lines) for the SCd structure at $\varepsilon = 0.83$, together with the corresponding errors when compared to a direct evaluation of the up-scaling problem (dots). Here the surrogate model has been constructed with $N = 10^3$ quasi-random samples generated from a Sobol sequence over the sampling space

$$(\varepsilon, Pe_d, Ki_d) \in [0.6, 0.95] \times [10^{-2}, 10^2] \times [10^{-2}, 10^2], \qquad [72]$$

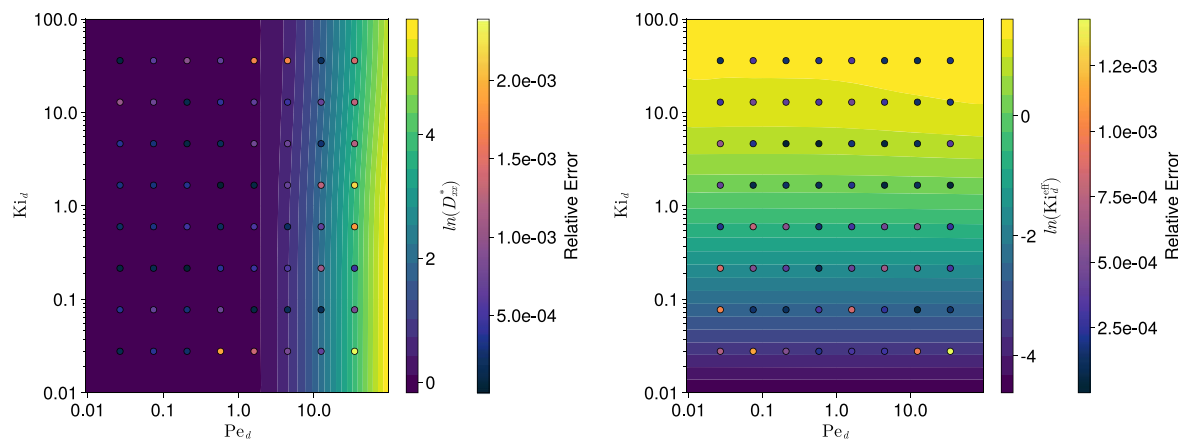which allows for an approximation with a relative error on the order of $O(10^{-3})$.

Figure 17. Predictions of the effective dispersion (left) and effective kinetic number (right) using the surrogate model, including the prediction error evaluated on a regular grid.

Conclusions and Outlook

Summary.—In this work, we presented an application of the VAM to the mass transport in PEs with a BV type electrochemical reaction. The simplifying assumptions allowed a reduction of the coupled transport problem to a single advection-diffusion equation coupled to a linear reaction law by using a suitable variable transformation.

We performed a dimensional analysis of the transport problem, which revealed the critical transport scaling parameters Pe_d, Ki_d, Sc, where we fixed Sc = 1000 in this study. Subsequently, we analyzed the highly non-linear dependency of the effective transport parameters $K_{d,xx}$, D_{xx}^*, and Ki_d^{eff} on the scaling parameters and the geometry, for which we studied two 2D and four 3D periodic structures parameterized by the porosity.

Validation studies for the predicted effective transport parameters showed good agreement with published results. Furthermore, the numerical studies revealed the predicted permeability value for the investigated structures to be in a realistic range when compared to simulation results of technical felt electrodes performed by Kok et al.[28] We challenged the periodicity assumption of the VAM by comparing simulation results at higher flow rates with the DNS approach. As expected, the VAM approach fails to predict accurate concentration profiles close to the macroscopic boundary for larger Péclet number values, which is due to the underlying assumption of a spatially periodic solution that neglects the influence of macroscopic boundary conditions. A detailed analysis of conditions for the validity of homogeneous macroscopic descriptions of reactive mass transport has been provided in Ref. 73.

The results presented in this work indicate that the ubiquitous usage of the analytical Bruggeman relation for the effective diffusion should be used with care when applied to FB applications as the relation neglects the effect of the PE geometry, heterogeneous reactions and convective flow on the effective total dispersion tensor.

In real-world engineering settings, such as fuel cells and flow batteries, porous electrode materials are sought that simultaneously exhibit high permeability and mass transfer rates, which itself is a highly relevant optimisation topic.[58] Here, we applied the evaluated effective parameters for a simple 1D macroscopic transport problem through a porous electrode, for which we determined the overall spatially averaged reaction rate and energy dissipation. This allowed to elucidate the trade-off between mass transport and energy dissipation for the considered pore-scale structures and porosity values. The results indicate that the optimal pore-scale structure depends on the operating conditions, where fibers aligned orthogonally to the convective flow direction are preferred at lower flow rates and fibers aligned parallel to the flow are preferred at higher flow rates. Additionally, the optimal porosity value was found to correlate inversely with the energy dissipation rate.

Finally, we constructed a surrogate model based on the Kriging method, which allows for an efficient evaluation of the effective transport numbers for a given set of dimensionless transport and geometrical parameters. The surrogate model is especially useful in case of inhomogeneous materials with spatially or temporally varying properties, for which the effective parameters must be evaluated over a range of transport parameters. We published a reduced porous electrode model as open-source software,[72] which allows for an efficient usage of the effective porous electrode parameters in macroscopic porous electrode models.

Since models using simple pore-scale geometries have been shown to often well-describe experimental data of more complicated geometries,[35] we consider this paper to be a valuable contribution to modeling the macroscopic reactive mass transport through porous electrodes in flow batteries.

Further research.—Further studies could explore the application of the VAM to non-linear reaction laws, where the conductivity in the electrolyte and solid electrode phase are taken into account.

Additionally, the inclusion of non-ideal effects of highly concentrated electrolytes, which are typical in industrial FB applications, would be a valuable extension. Furthermore, the consideration of more complex pore-scale geometries and anisotropy, based e.g. on micro CT scans, would be highly relevant to bridge the gap between the highly simplified structures considered in this study and technical porous electrode structures.

This study lays the groundwork for future research on the design of porous electrodes, such as gradient or lamellar materials, tailored for particular applications in electrochemistry. Through experimental validation of our findings, it would be possible to expand upon this study and establish guidelines for the manufacturing of porous electrodes.

ORCID

Jakub K. Wlodarczyk https://orcid.org/0000-0002-7269-983X
Roman P. Schärer https://orcid.org/0000-0001-9758-9234
Jürgen O. Schumacher https://orcid.org/0000-0002-8190-6773

References

1. E. Sánchez-Díez et al., "Redox flow batteries: status and perspective towards sustainable stationary energy storage." *Journal of Power Sources*, **481**, 228804 (2021).
2. B. W. Zhang et al., "A two-dimensional model for the design of flow fields in vanadium redox flow batteries." *Int. J. Heat Mass Transf.*, **135**, 460 (2019).
3. Q. Xu and T. S. Zhao, "Fundamental models for flow batteries." *Prog. Energy Combust. Sci.*, **49**, 40 (2015).
4. R. Wang et al., "Achieving gradient-pore-oriented graphite felt for vanadium redox flow batteries: meeting improved electrochemical activity and enhanced mass transport from nano- to micro-scale." *J. Mater. Chem. A*, **7**, 10962 (2019).
5. A. Forner-Cuenca and F. R. Brushett, "Engineering porous electrodes for next-generation redox flow batteries: Recent progress and opportunities." *Current Opinion in Electrochemistry*, **18**, 113 (2019).
6. V. A. Beck et al., "Computational design of microarchitected porous electrodes for redox flow batteries." *Journal of Power Sources*, **512**, 230453 (2021).
7. H. R. Jiang et al., "A gradient porous electrode with balanced transport properties and active surface areas for vanadium redox flow batteries." *Journal of Power Sources*, **440**, 227159 (2019).
8. B. Tjaden et al., "On the origin and application of the Bruggeman correlation for analysing transport phenomena in electrochemical systems." *Current Opinion in Chemical Engineering*, **12**, 44 (2016).
9. D.-W. Chung et al., "Validity of the Bruggeman relation for porous electrodes." *Modelling Simul. Mater. Sci. Eng.*, **21**, 074009 (2013).
10. K. Oh et al., "Three-dimensional, transient, nonisothermal model of all-vanadium redox flow batteries." *Energy*, **81**, 3 (2015).
11. X. You et al., "2-D Model of a H2/Br2 Flow Battery with Flow-Through Positive Electrode." *J. Electrochem. Soc.*, **163**, A447 (2016).
12. D. Li, "Phase diagrams and thermochemical modeling of salt lake brine systems." *I. LiCl+H2O system*, **51**, 1 (2015).
13. U. D. Schiller and F. Wang, "Multiscale simulation of transport phenomena in porous media: From toy models to materials models." *MRS Commun.*, **8**, 358 (2018).
14. D. Kehrwald et al., "Local tortuosity inhomogeneities in a lithium battery composite electrode." *J. Electrochem. Soc.*, **158**, A1393 (2011).
15. T. D. Le et al., "Multi-scale modeling of diffusion and electrochemical reactions in porous micro-electrodes." *Chemical Engineering Science*, **173**, 153 (2017).
16. J. Newman and W. Tiedemann, "Porous-electrode theory with battery applications." *AIChE J.*, **21**, 25 (1975).
17. B. K. Chakrabarti et al., "Modelling of redox flow battery electrode processes at a range of length scales: A review." *Sustainable Energy Fuels*, **4**, 5433 (2020).
18. O. C. Esan et al., "Modeling and simulation of flow batteries." *Adv. Energy Mater.*, **10**(31) 2000758 (2020).
19. X. Ke et al., "Redox flow batteries with serpentine flow fields: Distributions of electrolyte flow reactant penetration into the porous carbon electrodes and effects on performance." *Journal of Power Sources*, **384**, 295 (2018).
20. A. Gayon Lombardo et al., "A pore network model of porous electrodes in electrochemical devices." *Journal of Energy Storage*, **24**, 100736 (2019).

21. Q. Chen et al., "Dissection of the voltage losses of an acidic quinone redox flow battery." *J. Electrochem. Soc.*, **164**, A1126 (2017).
22. Q. Wang et al., "Numerical study on vanadium redox flow battery performance with non-uniformly compressed electrode and serpentine flow field." *Appl. Energy.*, **220**, 106 (2018).
23. C. Ma et al., "A two-dimensional porous electrode model for designing pore structure in a quinone-based flow cell." *J. Energy Storage.*, **18**, 16 (2018).
24. G. Wang et al., "Direct numerical simulation (DNS) modeling of PEFC electrodes." *Electrochimica Acta.*, **51**, 3139 (2006).
25. S. Jung, "Computational study about the effect of electrode morphology on the performance of lithium-ion batteries." *Int. J. Energy Res.*, **40**, 1073 (2016).
26. A. Xu et al., "Lattice Boltzmann modeling of transport phenomena in fuel cells and flow batteries." *Acta Mech. Sin.*, **33**, 555 (2017).
27. G. Qiu et al., "3-D pore-scale resolved model for coupled species/charge/fluid transport in a vanadium redox flow battery." *Electrochimica Acta.*, **64**, 46 (2012).
28. M. D. R. Kok et al., "Mass transfer in fibrous media with varying anisotropy for flow battery electrodes: Direct numerical simulations with 3D X-ray computed tomography." *Chemical Engineering Science*, **196**, 104 (2019).
29. D. Zhang et al., "The effect of wetting area in carbon paper electrode on the performance of vanadium redox flow batteries: a three-dimensional lattice Boltzmann study." *Electrochimica Acta.*, **283**, 1806 (2018).
30. D. Zhang et al., "Understanding the role of the porous electrode microstructure in redox flow battery performance using an experimentally validated 3D pore-scale lattice Boltzmann model." *Journal of Power Sources*, **447**, 227249 (2020).
31. M. A. Sadeghi et al., "Exploring the impact of electrode microstructure on redox flow battery performance using a multiphysics pore network model." *J. Electrochem. Soc.*, **166**, A2121 (2019).
32. R. Banerjee et al., "Characterization of carbon felt electrodes for vanadium redox flow batteries - A pore network modeling approach." *Journal of Energy Storage*, **21**, 163 (2019).
33. Y. Davit et al., "Homogenization via formal multiscale asymptotics and volume averaging: How do the two techniques compare?" *Advances in Water Resources*, **62**, 178 (2013).
34. I. Battiato et al., "Theory and applications of macroscale models in porous media." *Transp Porous Med.*, **130**, 5 (2019).
35. S. Whitaker, "The method of volume averaging." *Theory and Applications of Transport in Porous Media* (Springer, Netherlands) Vol. 13 (1999).
36. B. D. Wood, "The role of scaling laws in upscaling." *Advances in Water Resources*, **32**, 723 (2009).
37. F. J. Valdés-Parada et al., "On diffusion, dispersion and reaction in porous media." *Chemical Engineering Science*, **66**, 2177 (2011).
38. F. Golfier et al., "Heat and mass transfer in tubes: an analysis using the method of volume averaging." *JPM*, **5**, 7 (2002).
39. K. R. Rushton, *Groundwater Hydrology: Conceptual and Computational Models* (The United Kingdom)(Wiley) 1st ed. (2003).
40. M. Agnaou et al., "Origin of the inertial deviation from Darcy's law: An investigation from a microscopic flow analysis on two-dimensional model structures." *Phys. Rev. E*, **96**, 043105 (2017).
41. W. W. Wallender and D. Buyuktas, "Dispersion in spatially periodic porous media." *Heat Mass Transf.*, **40**, 261 (2004).
42. F. J. Valdés-Parada et al., "Diffusion and heterogeneous reaction in porous media: the macroscale model revisited." *Int. J. Chem. React. Eng.*, **15**, 7 (2017).
43. H. D. Lugo-Méndez et al., "Upscaling diffusion and nonlinear reactive mass transport in homogeneous porous media." *Transp Porous Med.*, **107**, 683 (2015).
44. J. Guo et al., "Dispersion in porous media with heterogeneous nonlinear reactions." *Transp Porous Med.*, **109**, 541 (2015).
45. E. J. F. Dickinson and A. J. Wain, "The Butler-Volmer equation in electrochemical theory: Origins, value, and practical application." *Journal of Electroanalytical Chemistry*, **872**, 114145 (2020).
46. S. Whitaker, "The Forchheimer equation: A theoretical development." *Transp Porous Med.*, **25**, 27 (1996).
47. R. Carta et al., "Behaviour of a carbon felt flow by electrodes Part I: Mass transfer characteristics." *J Appl Electrochem.*, **21**, 793 (1991).
48. A. J. Bard and L. R. Faulkner, *Electrochemical Methods: Fundamentals and Applications, 2nd Edition* (Wiley) (2000).
49. A. Z. Weber et al., "Redox flow batteries: a review." *J Appl Electrochem.*, **41**, 1137 (2011).
50. T. Tichter et al., "Finite heterogeneous rate constants for the electrochemical oxidation of $VO2+$ at glassy carbon electrodes." *Front. Energy Res.*, **8**, 155 (2020).
51. B. Huskinson and M. J. Aziz, "Performance model of a regenerative hydrogen bromine fuel cell for grid- scale energy storage." *Energy Sci. Technol.*, **5**(1), 16 (2013).
52. B. Huskinson et al., "A metal-free organic-inorganic aqueous flow battery." *Nature*, **505**, 195 (2014).
53. J. Cao et al., "A highly reversible anthraquinone-based anolyte for alkaline aqueous redox flow batteries." *J. Power Sources*, **386**, 40 (2018).
54. T. Liu et al., "A total organic aqueous redox flow battery employing a low cost and sustainable methyl viologen anolyte and 4-HO-TEMPO catholyte." *Adv. Energy Mater.*, **6**, 1501449 (2016).
55. C. Beriet and D. Pletcher, "A further microelectrode study of the influence of electrolyte concentration on the kinetics of redox couples." *Journal of Electroanalytical Chemistry*, **375**, 213 (1994).
56. D. Aaron et al., "Polarization curve analysis of all-vanadium redox flow batteries." *J Appl Electrochem*, **41**, 1175 (2011).
57. J. D. Milshtein et al., "Quantifying mass transfer rates in redox flow batteries." *J. Electrochem. Soc.*, **164**, E3265 (2017).
58. A. Xu et al., "Lattice boltzmann simulation of mass transfer coefficients for chemically reactive flows in porous media." *J. Heat Transf.*, **140**, 052601 (2018).
59. I. V. Zenyuk et al., "Gas-diffusion-layer structural properties under compression via X-ray tomography." *Journal of Power Sources.*, **328**, 364 (2016).
60. K. Yazdchi et al., "Microstructural effects on the permeability of periodic fibrous porous media." *International Journal of Multiphase Flow*, **37**, 956 (2011).
61. A. Eidsath et al., "Dispersion in pulsed systemsIII: Comparison between theory and experiments for packed beds." *Chemical Engineering Science*, **38**, 1803 (1983).
62. I. Frankel and H. Brenner, "On the foundations of generalized Taylor dispersion theory." *J. Fluid Mech.*, **204**, 97 (1989).
63. M. A. Hamid and K. C. Smith, "Modeling the transient effects of pore-scale convection and redox reactions in the pseudo-steady limit." *J. Electrochem. Soc.*, **167**, 013521 (2020).
64. N. Luminari et al., "Effects of porosity and inertia on the apparent permeability tensor in fibrous media." *International Journal of Multiphase Flow*, **106**, 60 (2018).
65. R. Schulz et al., "Beyond kozeny-carman: predicting the permeability in porous media." *Transp Porous Med.*, **130**, 487 (2019).
66. N. Takano et al., "Microstructure-based evaluation of the influence of woven architecture on permeability by asymptotic homogenization theory." *Composites Science and Technology*, **62**, 1347 (2002).
67. K. Yazdchi et al., "Micro-macro relations for flow through random arrays of cylinders." *Composites Part A: Applied Science and Manufacturing*, **43**, 2007 (2012).
68. L. Falk and J. M. Commenge, "Performance comparison of micromixers." *Chemical Engineering Science*, **65**, 405 (2010).
69. D. R. Jones and M. Schonlau, "Efficient Global Optimization of Expensive Black-Box Functions." *Journal of Global Optimization*, **13**, 455 (1998).
70. D. R. Jones, "A taxonomy of global optimization methods based on response surfaces." *Journal of Global Optimization*, **21**, 345 (2001).
71. SciML/Surrogates.jl. 2023 SciML Open Source Scientific Machine Learning, p. 34. https://github.com/SciML/Surrogates.jl (Sept. 28, 2023).
72. R. P. Schaerer and J. K. Wlodarczyk, (2022), SEMCs, the simplified volume-averaged electrode model for the use in continuum scale RFB models. https://github.com/Isomorph-Electrochemical-Cells/RFB-SEMCS.
73. I. Battiato and D. Tartakovsky, "Applicability regimes for macroscopic models of reactive transport in porous media." *Journal of Contaminant Hydrology*, **120-121**, 18 (2011).